![ndc logo]

TEXTURE IN TUBES AND PLATES OF NITINOL

Robertson, Imbeni, Notkina, Wenk, Ritchie

Proceedings of the International Conference on Shape Memory and Superelastic Technologies, SMST-2003

2003

SMST-2003

Proceedings of the International Conference on

Shape Memory and Superelastic Technologies

5 May to 8 May 2003
Asilomar Conference Center
Pacific Grove, California, USA

Editors
Alan R. Pelton
Tom Duerig

TEXTURE IN TUBES AND PLATES OF NITINOL

S.W. Robertson,[1] V. Imbeni,[2] E. Notkina,[3] H.-R. Wenk,[4] and R.O. Ritchie[1]

[1]*Materials Sciences Division, Lawrence Berkeley National Laboratory,
and Department of Materials Science and Engineering, University of California, Berkeley*
[2]*SRI International and The International Organization
on Shape Memory and Superelastic Technologies*
[3]*Technische Universität Hamburg-Harburg, Hamburg, Germany*
[4]*Department of Geology and Geophysics, University of California, Berkeley*

ABSTRACT

The superelastic/shape memory material, Nitinol, a roughly equiatomic alloy of Ni and Ti, rapidly is becoming one of the most important metallic implant materials in the biomedical industry, in particular for the manufacture of endovascular stents. As such stents invariably are laser machined from Nitinol tubes (or sheets rolled into tubes), it is important to understand fully the physical phenomena that may affect the mechanical behavior of this material. With tubing and sheet, one major issue is crystallographic texture, which can play a key role in influencing the mechanical properties of Nitinol. In this paper, we present a preliminary study on how geometry and heat treatment can affect the texture of Nitinol.

KEYWORDS

Nitinol, Texture, X-ray Diffraction, Pole Figures

INTRODUCTION

The production of biomedical devices made from the shape memory and superelastic alloy Nitinol, a roughly equiatomic alloy of Ni and Ti, employs numerous processing techniques, e.g. tube drawing, plate rolling, etc., and heat-treatment processes in order to modify the microstructure, transformation temperatures, and mechanical properties. These procedures can lead to texturing (crystallographic alignment) of the material. There are a few, mainly qualitative, reports of textures in Nitinol sheets and plates [1–8] but no information for textures of tubes. Since Nitinol derives its unique nonlinear and anisotropic mechanical behavior from stress-induced martensitic transformations, where the resulting strains are affected by crystallographic orientation, it is clear that texture can have a marked influence on its mechanical properties. Indeed, Gall and Sehitoglu [9] have concluded that texture, and consequently variants of martensite active during the transformation, are the source of the compression-tension asymmetry of Nitinol. Furthermore, Vaidyanathan *et al.* [10]

have concluded that texturing can occur in Nitinol when martensite is stress induced from austenite via such compression loading. Texture can have a critical effect in modeling the constitutive behavior of the alloy, as shown in Figure 1 [11] where the assumption of the correct texture is shown to influence markedly the finite element predictions of the equivalent stress-equivalent strain curve for Nitinol under combined tensile and torsional loading and unloading.

It is the goal of this preliminary study to understand better how processing and heat treatment affect the texture in Nitinol, specifically by examining drawn tubes in comparison to rolled plate. The motivation for this comparison is to determine if such tubes could be simply modeled as plates rolled into a cylindrical form. This can be important when the flat geometry of plate specimens is preferred over a curved geometry for certain testing conditions, such as for microscopy studies which require a flat surface for resolution.

MATERIALS AND EXPERIMENTAL PROCEDURES

Nitinol tubing and plate (50.8 at.%Ni,) was received from Nitinol Devices & Components, Inc. and heat-treated, as described below, to modify the microstructure. The sample geometries (tube vs. plate) were chosen to determine if the processing (drawing vs. rolling) has a significant effect on the texture. The samples were heat treated to two different specifications:

• 485°C in air furnace for 5 min., followed by an ice-water quench (on both tube and plate).

• 850°C *in vacuo* furnace for 30 min. followed by a slow cool (on plate only).
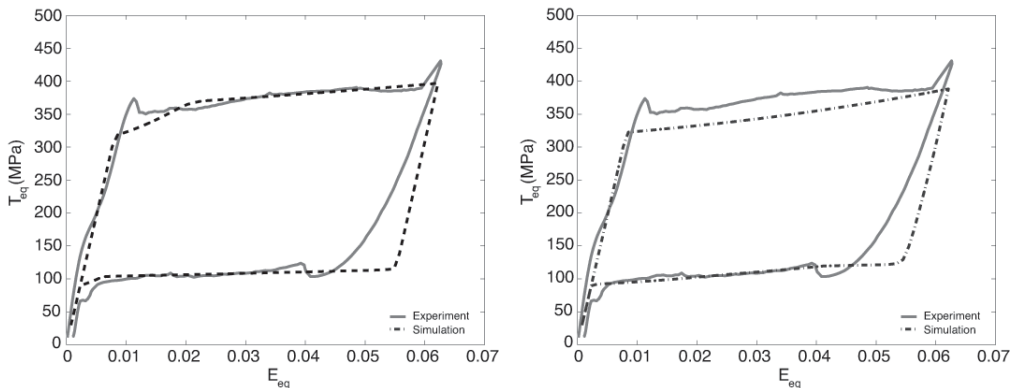
Figure 1 Finite element simulation curves of equivalent stress vs. equivalent strain for Nitinol tubing under combined tension and torsion loading conditions (a) assuming the correct texture of the tubes, and (b) assuming incorrect texture [11].

The tube dimensions were 4.6 mm outer diameter and 3.9 mm inner diameter; the plate sections were 15 mm square by 1 mm thick. The samples were deformed too heavily for SEM-EBSP texture measurements and therefore textures were measured with an X-ray pole figure goniometer. To provide large enough samples, the tube was sliced into sections (see Figure 2) and the sections were lined up side-by-side, cold mounted in epoxy, and ground flat. Figure 2 shows that two slice types were used, an offset cross-section (maximized geometry with minimum sample) and a pure radial cross-section (ideal axial alignment for easier pole figure interpretation). After combining the multiple tube slices into two samples, their sizes were approximately 10 mm square, the minimum sam-

Figure 2 Diagram of slices from tube taken for texture measurements at a) offset cross-section and b) pure radial cross-section.

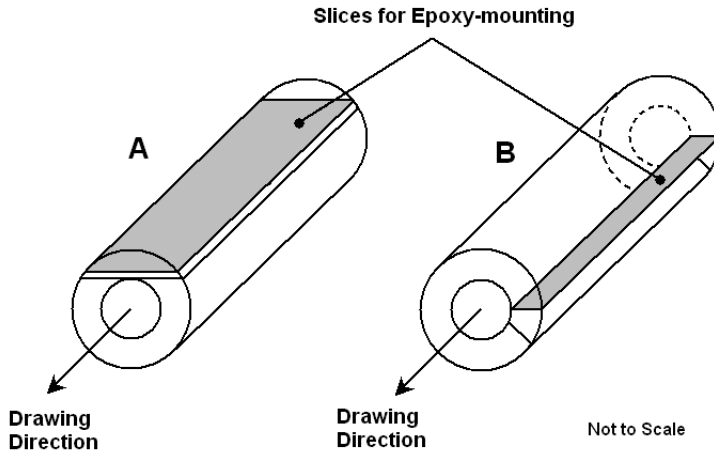ple size for quantitative texture analysis with an X-ray pole figure goniometer. All samples were mechanically ground and polished to a 0.05 μm finish to permit X-ray diffraction and establish consistency among the samples.

Both the tube and plate samples were fully austenitic at room temperature, i.e. the $A_f < 25°C$. Optical micrographs of the microstructure are shown in Figure 3. It should be noted that the imaged martensitic grains in the 485°C heat-treated samples are polishing artifacts; stresses from grinding and polishing cause transformation in the exposed grains, which leaves residual surface relief on etching. Moreover, for the as-drawn conditions, the apparent grain sizes observed in Figures 3a and 3b also give a false impression about the actual grain size; the true grain size for the as-drawn or rolled tube and plate is on a submicron scale and can only be revealed by transmission electron microscopy [12]. On the other hand, the optical micrograph in Figure 3c is representative of the grain size of the fully annealed plate, as the annealing has allowed significant recrystallization and grain growth.
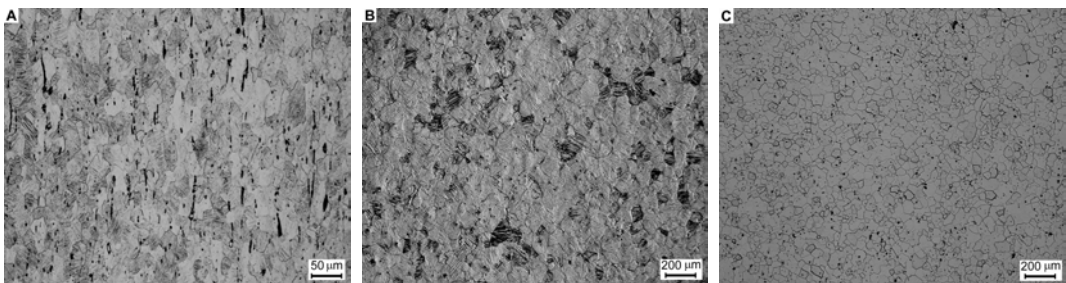

Figure 3 Optical micrographs of (a) tube heat treated at 485°C for 5 min.; drawing direction is vertical, (b) plate heat treated at 485°C for 5 min., and (c) plate heat treated at 850°C for 30 min.

The crystallographic texture of the Nitinol was determined from three incomplete measured pole figures (110, 200, and 211 poles at θ^1 values of 21.3°, 30.8°, and 38.9°, respectively) and using the WIMV[1] method in BEARTEX[1] to obtain the Orientation Distribution Function (ODF) [13]. Pole figures were measured with a Huber X-ray pole figure goniometer with Cu-Kα radiation source at 40 kV and 14 mA and a graphite monochromator. From the ODF, pole figures for 100, 110, and 111 poles were recalculated following smoothing and rotation operations and are presented in the following section, together with ODF sections.

RESULTS AND DISCUSSION

Pole Figures

The pole figures in Figure 4 reveal that the tube and plate heat treated at 485°C show a significant texture. After corresponding rotations, pole figures derived from both sections of the 485°C heat-treated tube are similar (see Figures 4a and 4b). The main feature is a maximum in the 111 pole in the circumferential direction as indicated by the dark spots at 6 and 12 o'clock in Figures 4a and 4b, pole direction (p.d.) 111. In addition, texture minima occur in the 100 pole parallel to all three primary directions (drawing, circumferential, and radial) as indicated by white areas in Figures 4a and 4b, p.d. 100, at 3 and 9 o'clock, 6 and 12 o'clock, and center, respectively. The pole figure of the pure radial cross-sectioned tube, Figure 4b, shows a weak tendency in the 111 pole parallel to the radial direction.

The 485°C heat-treated plate displays a maximum in the 110 pole parallel to the rolling direction, as indicated by the highest intensity at 3 and 9 o'clock in Figure 4c, p.d. 110. Also, there is a 111 maximum parallel to the normal direction as shown by the dark-spot concentration at the center of Figure 4c, p.d. 111. Furthermore, the 485°C heat-treated plate has texture minima at the 100 and 111 poles parallel to the rolling direction as indicated by white areas at 3 and 9 o'clock in Figures 4c, p.d. 100, and 4c, p.d. 111. Another minimum was observed at the 110 pole parallel to the normal (thickness) direction as indicated by the white spot in the center of Figure 4c, p.d. 110. The pole figures for this plate are consistent with Body-Centered Cubic (BCC) rolling textures [12].

Pole figures of the 850°C heat-treated plate show stochastic variations due to poor grain statistics (see Figure 4d). A more regular pattern becomes apparent after additional smoothing (see Figure 4e). Scattering of the data in Figure 4d is attributed to recrystallization and grain growth experienced during the annealing. Figure 4e shows that the 850°C heat-treated texture is generally the same as that of the plate heat-treated at 485°C, although the degree of texturing was much less in the higher temperature heat-treated condition, as indicated by the lower pole densities (the same contouring levels were used for all pole figures).

The only apparent similarity between Nitinol tube and plate texture is the minimum of the 100 pole in the rolling/drawing direction. There may also be a correlation between the tube's weak, and the plate's strong, tendency to texture the 111 pole in the radial/normal direction. The significant differences in texture indicate that plate should not be used as a replacement for tubes when tests are geometry limited. Moreover, plates that have been folded into a cylinder may not be assumed to have the same texture as tubes.

---

[1] θ is equal to half of the angle between the X-ray source and detector; WIMV calculates orientation distributions from pole figures; BEARTEX is a software package for quantitative texture analysis.

The observed plate textures in Figures 4c–4e were similar to those previously determined by Monasevich et al. [1], Li et al. [2], and Inoue et al. [4] on other Nitinol plate or sheet geometry. However, pole figures calculated by Kitamura et al. [5] were different than those obtained in this study. Their work on much thinner Nitinol sheets (0.1 mm) revealed a texture maximum of the 110 pole normal to the sheet, whereas our data indicated a texture minimum at that location. That group also observed that, upon increased-temperature heat treatment (400°C vs. 600°C, both for 60 min.), maximum intensities of the 110 pole in the rolling direction diffuse toward the transverse direction creating offset local maxima. This trend was also observed in the pole figures collected in our experiment; notice how the maximum intensity spots at 3 and 9 o'clock in the 485°C heat-treated plate (Figure 4c, p.d. 110) diffuse into four spots in the plate heat treated at 850°C (Figure 4e, p.d. 110).
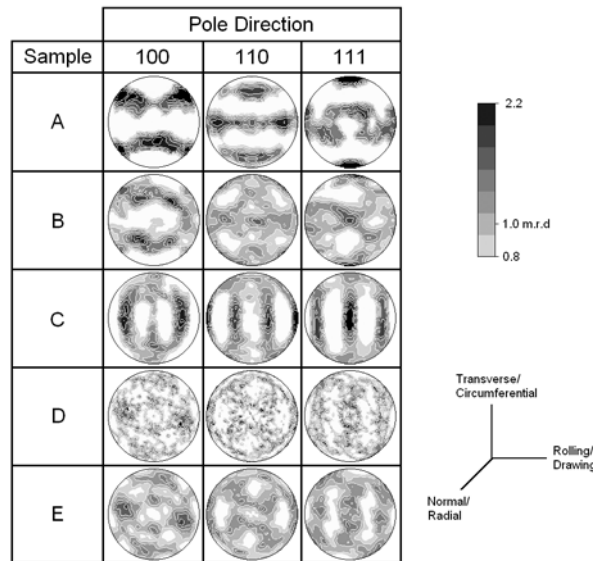

Figure 4 Pole figures showing texture in (a) 485° C H.T. tube offset cross-section, (b) 485° C H.T. tube pure radial cross-section, (c) 485° C H.T. plate, (d) 850° C H.T. plate with one ODF smoothing operation (same as a–c), and (e) 850° C H.T. plate with three ODF smoothing operations.

Sample Orientation Distributions (SODs)

In order to obtain further information on texture components, the ODF was analyzed in Sample Orientation Distribution (SOD) sections, displaying sample orientations in terms of crystal coordinates φ_1 and Φ (Bunge nomenclature is used). Figure 5 shows four SOD sections at φ_1 values of 0, 15, 30, and 45 degrees for the 485°C heat-treated tube and plate. The plate shows the typical features of a BCC rolling texture with α fiber in the $\varphi_1=0°$ section and a γ fiber extending parallel to φ_1 [14].

In the tube sample, the α fiber is absent and the γ fiber is developed only weakly. The most pronounced orientation concentration, labeled as point A in the figure, is in the $\varphi_1=45°$ section at $\Phi=90°$ and $\varphi_1=45°$. Interpretations of the details contained in each SOD section is beyond the

scope of this preliminary investigation but will be conducted in future studies to completely characterize the tube texture and understand its development.

The results presented in this report are based upon pole figure collection of one sample of each selected geometry and heat treatment. Future experiments are needed to confirm the findings presented here and to further investigate the influence of deformation conditions on texture and also on texture changes during the phase transformation.
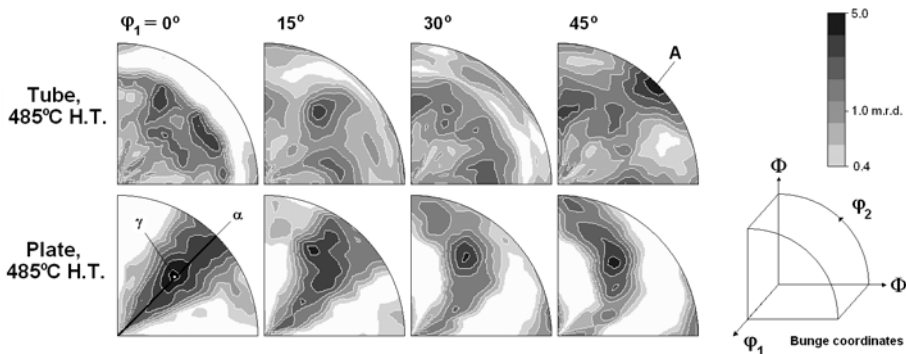

Figure 5 SODs for 485° C heat-treated tube (pure radial cross-section) and plate in polar coordinates; point A is the most pronounced texture component for the tube. The α fiber, and γ fiber for the plate are indicated.

PRELIMINARY OBSERVATIONS

Room-temperature fully austenitic Nitinol tubes and plates have been shown to be highly susceptible to crystallographic texturing following mechanical processing (drawing or rolling) and heat treatment. Specific conclusions include the following:

- The tubes were found to be textured strongly in the 111 pole, along the circumferential direction. They have a weak tendency to texture the 111 pole in the radial direction. Also, the tubes have texture minima of the 100 pole in the circumferential, drawing, and radial directions.

- The plates correspondingly were found to be textured with α and γ fibers, both common in BCC rolling textures. α fibers produce 110 poles parallel to the rolling/drawing direction, whereas the γ fiber is characterized by the 111 pole parallel to the normal direction (i.e. plate thickness). Texture minima occur in both the 100 and 111 poles parallel to the drawing direction and in the 110 pole parallel to the normal direction.

- Drawn tubes and rolled plates were observed to have few similarities in texture. We conclude therefore that plates should not be used as a substitute for tubes when testing is geometry limited. In addition, plates that have been rolled into a cylinder cannot be assumed to have the same texture as tubes.

- Some degree of remnant texture was found in Nitinol plate, even after a full anneal at 850°C for 30 min. This texture is similar to that of plate heat treated at 485° C for 5 min.

ACKNOWLEDGMENTS

REFERENCES

1.   L.A. Monasevich et al., in *Met. Sci. Heat Treat.* **21**, no. 9 (1979), p. 735.

2.   D.Y. Li, X.F. Wu, and T. Ko, in *Acta Metall. Mater.* **38** (1990), p. 19.

3.   J.H. Mulder, P.E. Thoma, and J. Beyer, in *Z. Metallkd.* **84** (1993), p. 501.

4.   H. Inoue, N. Miwa, and N. Inakazu, in *Acta Mater.* **44** (1996), p. 4825.

5.   K. Kitamura et al., in *SMST-97: Proceedings of the Second International Conference on Shape Memory and Superelastic Technologies,* eds. A. Pelton et al. (Pacific Grove, Calif.: International Organization on SMST), p. 47.

6.   Y.C. Shu and K. Bhattacharya, in *Acta Mater.* **46** (1998), p. 5457.

7.   E. Hornbogen, G. Bruckner, and G. Gottstein, in *Z. Metallkd.* **93** (2002), p. 3.

8.   H. Sitepu, W. Schmahl, and B. Von Dreele, in *Appl. Phys. A* **74** (2002), p. S1676.

9.   K. Gall and H. Sehitoglu, in *Int. J. Plasticity* **15** (1999), p. 69.

10. R. Vaidyanathan, M.A.M. Bourke, and D.C. Dunand, in *Metall. Mater. Trans. A* **32A** (2001), p. 777.

11. Y. Jung and P. Papadopoulos, "Constitutive Modeling and Numerical Simulation of Multivariant Phase Transformation in Shape Memory Alloys" *(*unpublished work, University of California, Berkeley*,* 2003).

12. Z.Q. Li and Q.P. Sun, in *Int. J. Plasticity* **18** (2002), p. 1481.

13. H.-R. Wenk, S. Matthies, J. Donovan, and D. Chateigner, in *J. Appl. Cryst.*, **31**, p. 262.

14. U.F. Kocks, C.N. Tome, and H.-R. Wenk, *Texture and Anisotropy* (Cambridge: Cambridge University Press, 1998), p. 195.

high temperature oxidation and the effects on corrosion are not entirely understood. This study investigates the phenomena of oxide formation by means of various surface analytical techniques and includes the exploration of oxidation kinetics as well as an assessment of the effects on biocompatibility.

EXPERIMENTAL METHODS AND TECHNIQUES

3-mm.-diameter Ni-50.8at.%Ti wire was annealed at 1000°C for 30 min., centerless ground to remove the resultant oxide scale, and electropolished. The wire was subsequently oxidized in an air furnace at 400–1000°C in 100°C increments for 3, 10, 30, 100, and 300 min. Auger Electron Spectroscopy (AES), Focused Ion Beam (FIB), JEOL JSM-5600 Scanning Electron Microscope (SEM), and Oxford Instruments Model 6587 Energy Dispersive X-Ray Spectroscopy (EDXS) were used to characterize the thickness and composition of the oxide layer(s). AES was used for oxide layers up to 0.1 μm, FIB between 0.1–1 μm, and SEM for 1 μm layers. Cross-sections of the wires were prepared using standard metallographic techniques. Two sections of wire from each heat-treatment condition were mounted in bakelite, polished to a mirrorlike finish with 60–1200 grit SiC paper, and cleaned in ultrasonicated denatured alcohol. Samples were not etched in order to ensure that all phases were retained for analysis.

Specimens were observed by SEM in both Secondary Electron Imaging (SEI) and Backscattered Electron Imaging (BEI) modes; the BEI mode was especially useful to differentiate Ni-rich (light) and Ti-rich (dark) phases. Layer-thickness measurements from AES were based on estimates from the FWHM depth profiles, whereas thicknesses from FIB and SEM were based on averages of measurements from several samples.

RESULTS AND DISCUSSION

Oxidation Growth and Composition

No visible oxide was observed by SEM for samples at lower temperatures (≤600°C) and at 700°C for shorter times (≤30 min.). These samples were analyzed with AES and/or FIB to determine the oxide thickness and composition. Figure 1 shows the AES depth profile of the electropolished and 400°C/3 min. samples, with a TiO_2 thickness of 110 Å and 200 Å, respectively. After 30 min. at 400°C, AES revealed a nickel-rich region beneath the outer TiO_2 layer (Figure 2). The remaining samples analyzed with AES showed a more pronounced nickel-rich region below the TiO_2 layer. Table 1 summarizes the oxide thicknesses as a function of temperature and time; the analytical technique used is also indicated

FIB [12] was used to analyze intermediate oxide thicknesses, as well as to overlap other analysis techniques. Figure 3 shows two light gray superficial platinum layers (marked) that are used as a protective coating during sample preparation. Beneath those layers, a darker TiO_2 (or other Ti suboxide layers) with a lighter nickel-rich sublayer is detected. Chuprina [7] also discovered a "white layer" beneath the surface scale by optical metallography, which he determined to be Ni_3Ti. Voids in the surface layers are also seen in Figure 3. The formation of voids and/or pores may be due to stress generation in the oxide during growth or by the Kirkendall effect whereby vacancies are created when the Ti atoms diffuse away from the NiTi matrix to react with O_2 [7,13–15]. Chu *et al.* [14] suggest that the formation of large voids may be due to the difference in the vertical and lateral oxide growth rates, as well as the collection of vacancies..
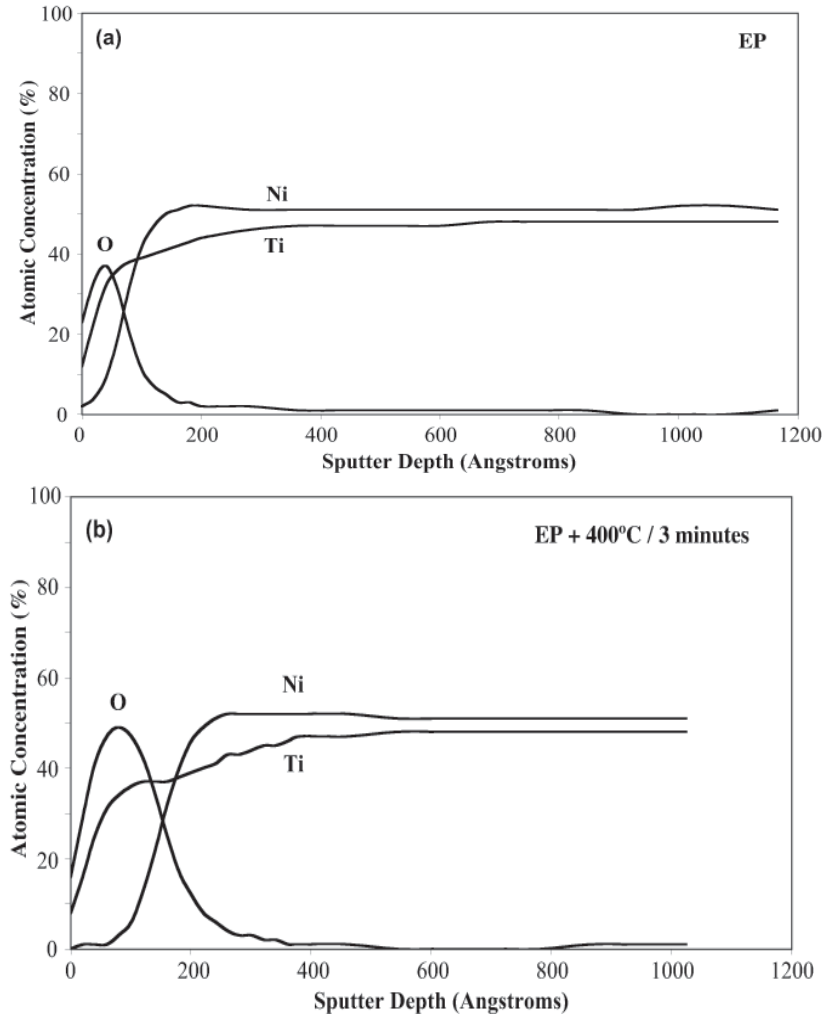
Figure 1 AES depth profiles of NiTi wire: (a) as electropolished; (b) 400°C for 3 min.

Figure 4 shows the cross-section of the as-electropolished wire, as compared to Figure 5, which illustrates the progressive growth of the oxide with increasing time at 900°C. The bright interfacial region between the base NiTi and the surface TiO$_2$ observed for the oxidized samples was analyzed by EDXS to be 75at.%Ni and 25at.%Ti, consistent with Ni$_3$Ti (white sublayer); EDXS also confirms the presence of TiO$_2$ (dark gray). Small Ni$_3$Ti fingerlike projections emerge from the nickel-rich layer and appear to form islands in the oxide. A comprehensive EDXS analysis indicates that the Ni content of the phases increases with increasing distance from the NiTi interface. The Ni$_3$Ti inter-facial layer transforms to Ni$_4$Ti (80at.%Ni), whereas the islands become nearly pure Ni (approxi-mately 92at.%Ni). This composition transition indicates that with increasing time at temperature, the Ni$_3$Ti sublayer becomes Ti-depleted as the Ti reacts with the O$_2$, leaving behind nearly pure Ni. The light gray areas embedded in the TiO$_2$ observed in Figure 5e may be NiO and TiO$_2$, which can react to form the double-oxide NiTiO$_3$ [16]. Other authors [7–9, 13–14] obtained similar results,
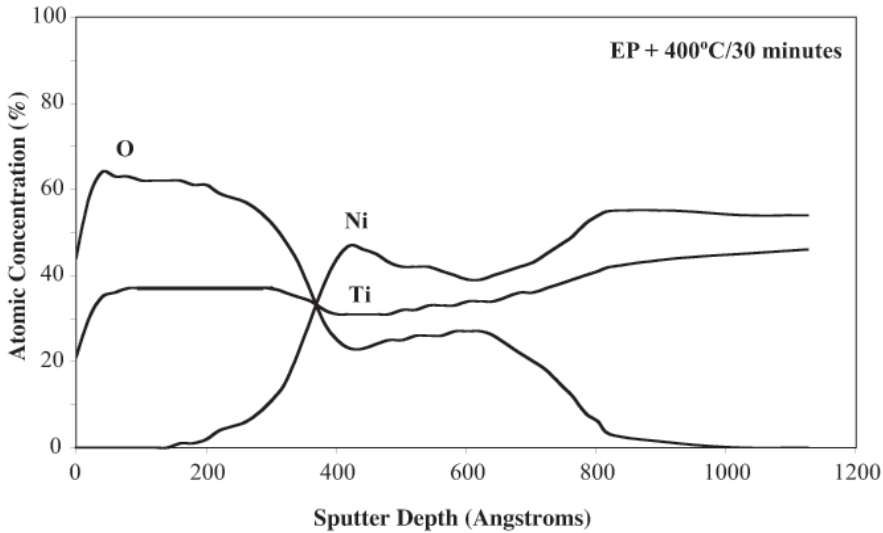
Figure 2 AES depth profile of 400° C/30 min. NiTi wire. Note the presence of a Ni-rich region below the TiO$_2$ surface layer.

Table 1 Oxide Thickness as a Function of Temperature and Time with Analytical Technique

Time (min.)	Temperature (°C)						
	400	500	600	700	800	900	1000
	Oxide Thickness (μm)						
0	0.0110 A	0.0110 A	0.0110 A	0.0110 A	0.0110 A	0.0110 A	0.0110 A
3	0.0200 A	0.0188 A	0.0338 A	0.180 A	2.737 S	6.052 S	11.23 S
10	0.0338 A	0.0244 A	0.0808 F	0.550 F	5.775 S	11.40 S	21.90 S
30	0.0282 A	0.0676 F	0.534 F	0.738 S	13.70 S	14.70 S	54.80 S
100	0.0470 F	0.0708 F	1.356 F	2.230 S	15.33 S	23.50 S	157 S
300	0.0670 F	0.0714 S	2.650 S	6.780 S	20.92 S	43.80 S	278 S

*Primary Analytical Technique: **A** = AES, **F** = FIB, and **S** = SEM

but there are discrepancies in the actual composition of these phases. X-ray diffraction analysis in Chuprina *et al.* showed the coexistence of Ni$_3$Ti, Ni, NiO, Ni(Ti), and TiO$_2$ at high temperatures (>600° C) [7]. Metallic Ni, oxidized Ni, or Ti atoms in solid solution with Ni (Ni(Ti)) have also been reported [9, 13–14].

After 3 min. at 1000° C, the nickel-rich and titanium oxide regions can be observed easily by BEI/SEM (see Figure 6a). The nickel-rich precipitates and TiO$_2$ form a lamellar structure of alternating Ni-rich phases and TiO$_2$. After 30 min. at 1000° C, this structure becomes more apparent (see Figure 6b), and after 300 min. at 1000° C, the oxide has become extremely thick (approximately 300 μm), with most of the Ni from Ni$_3$Ti dispersing into the TiO$_2$ layer (see Figure 6c). As Ni dif-
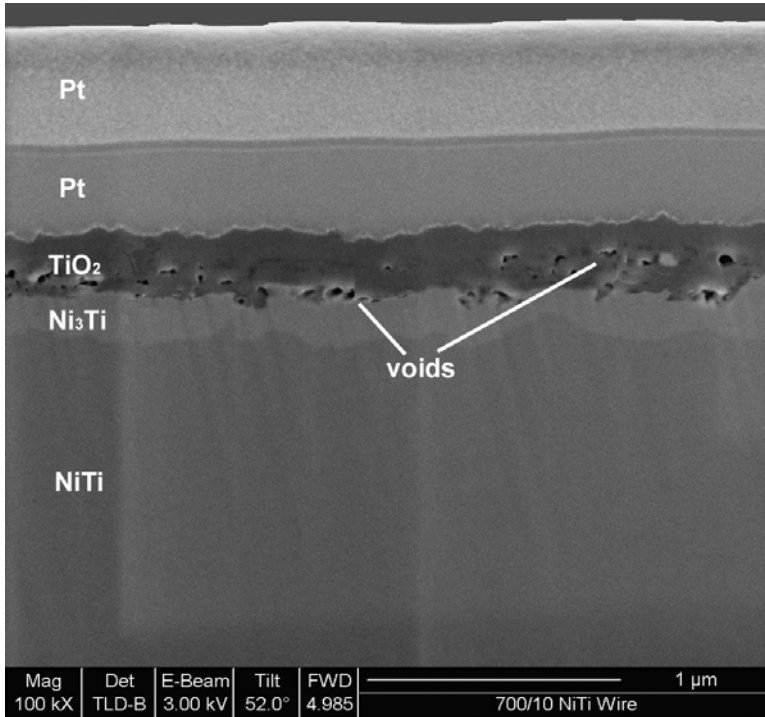
Figure 3   FIB image of 700° C/10 min. NiTi at 100,000×. Note the bright Ni$_3$Ti layer and (dark) voids.
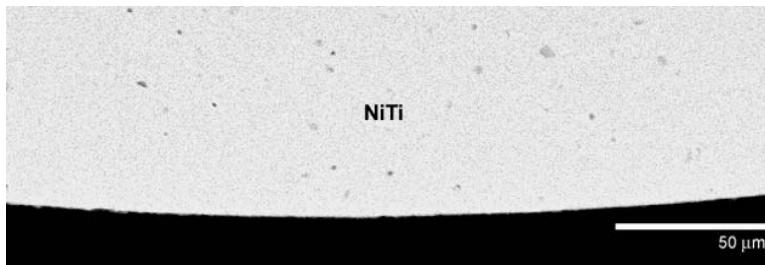
Figure 4   BEI/SEM image of as-electropolished cross-section (500×).

fuses to the surface, it becomes increasingly pure (approximately 98at.%Ni), with most of the Ti reacting with O$_2$ to form TiO$_2$.

It appears that the TiO$_2$ layer acts as a diffusion barrier to prevent Ni from oxidizing as expected from pure metal thermodynamics [17]. This is also consistent with the thermodynamic calculations from Firstov *et al*. [13], which indicate that reactions at the NiTi/air interface consist of NiTiO$_3$, TiO$_2$, and metallic Ni, whereas NiO would not be formed due to insufficient oxygen partial pressures.   Oxidation Kinetics.

Figure 7 illustrates the effect of time and temperature on oxide thickness from the present experimental study. Note that there is an initial high growth rate followed by slower growth kinetics at all temperatures. These data also demonstrate the expected trend of higher oxidation rates at higher
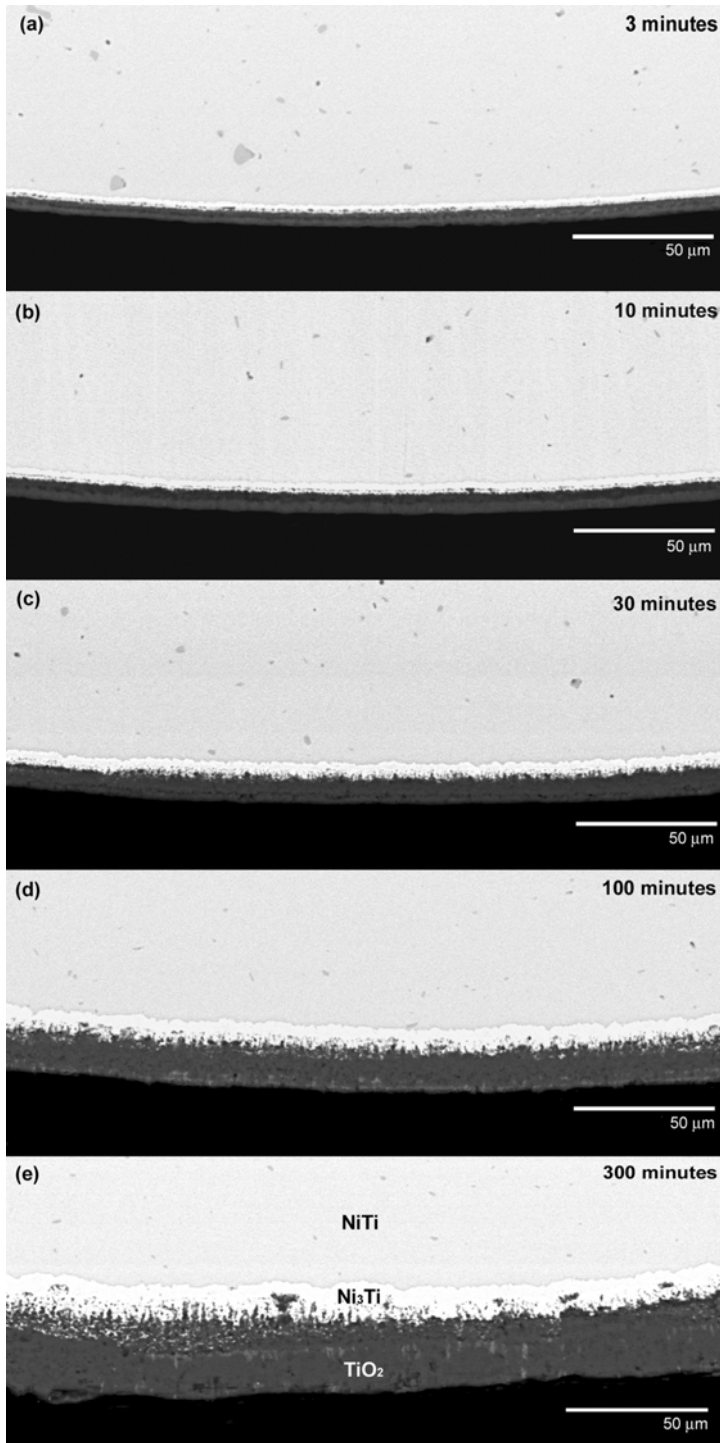
Figure 5 BEI/SEM images of NiTi wire cross-section after 900° C: (a) 3 min. (b) 10 min. (c)30 min. (d) 100 min. (e) 300 min. (500×).
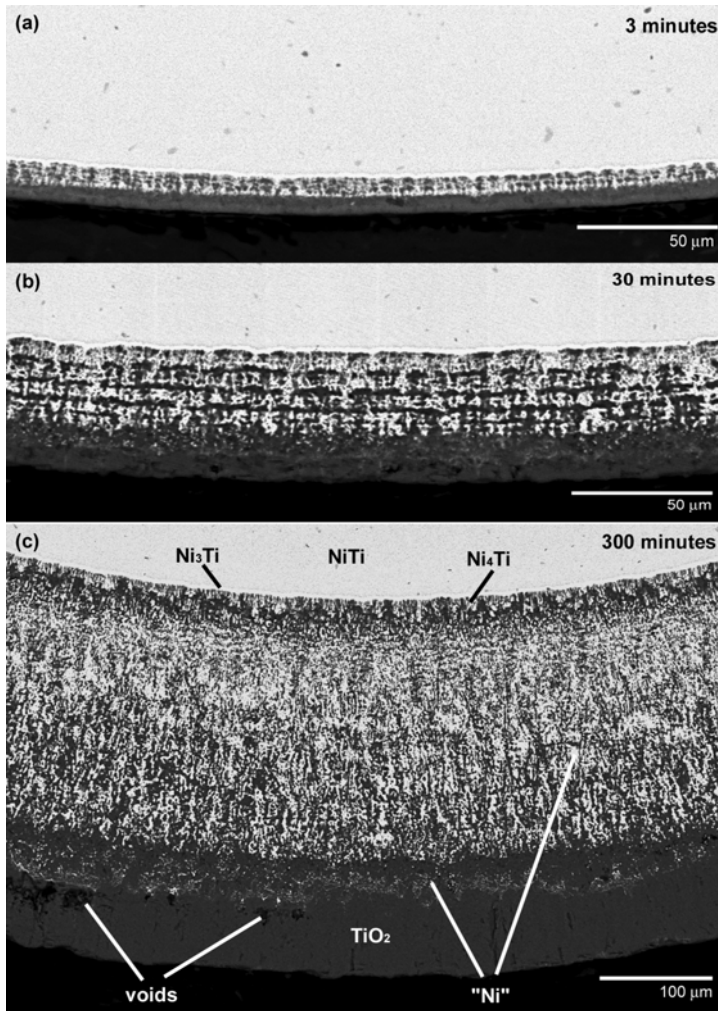
Figure 6 BEI/ SEM image of NiTi wire cross-section after electropolishing and a heat treatment at 1000° C: (a) 3 min. (500×), (b) 30 min. (500×), (c) 300 min. (200×).

temperatures. These observations are consistent with a model of oxygen absorption on the NiTi surface that reacts with outward diffusing Ti to form TiO_2. Chu *et al.* [14] and Keng *et al.* [16] discussed the relative direction of atomic diffusion and phase formation. During the early stages of oxidation, the growth of the TiO_2 layer is the only contributor to thickness and therefore oxide formation is relatively rapid. However, the preferential oxidation of Ti creates a Ti-depleted (Ni-rich) zone at the $NiTi/TiO_2$ interface as illustrated in Figures 3–6. The formation of the Ni-rich layer increases the effective diffusion distance with an associated decrease in overall oxidation kinetics. Continued oxide growth therefore involves simultaneous nucleation and growth of titanium oxides and Ni-rich phases. Ultimately, these processes lead to the formation of a protective oxide scale, which prevents further oxidation of the base material.Several authors observed parabolic oxidation rates in NiTi alloys [13–14, 16, 18]. The governing equation can be written as

Figure 7 The effect of time on oxide thickness is consistent with parabolic oxide growth.

$$thk^2 = k_p t \tag{1}$$

which indicates that square of the oxide thickness (thk^2) is proportional to time, *t*, through the parabolic oxidation rate, k_p. Oxidation rates were determined from the data shown in Figure 7. For illustrative purposes, these data were plotted on a log scale. These data can also be modeled with an Arrhenius equation, shown as equation 2, which governs the reaction rates.
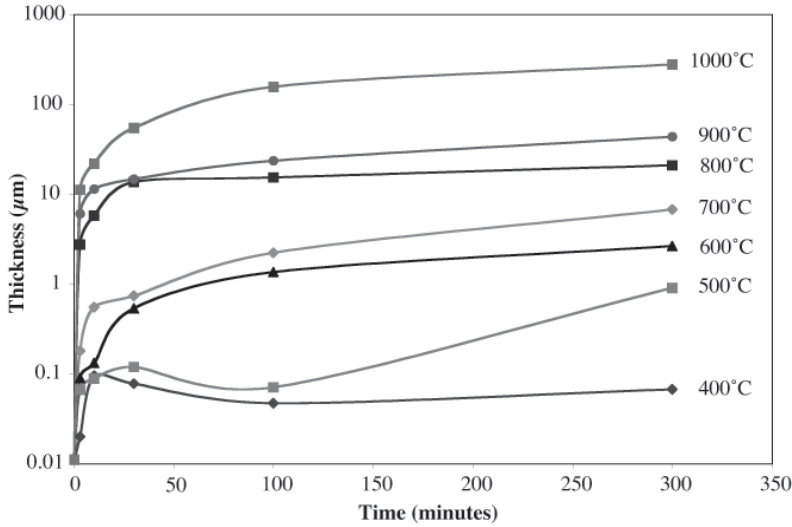
$$k_p = k_0 \, exp(-Q/RT) \tag{2}$$

where k_o is the rate constant, Q is the activation energy, R is the gas law constant, and T is the absolute temperature. Figure 8 plots the rate constant as a function of 1/T for the seven data sets. An activation energy of 50 kcal/mol was determined from the slope of the curve. This oxidation activation energy is the same order of magnitude as the activation energy to form NiO from pure Ni (45 kcal) and TiO_2 from pure Ti (26 kcal) [19]; these curves are also shown in Figure 8 for comparison. Chu *et al.* [14] obtained an activation energy of 54 kcal/mol (700–1000°C), which agrees well with the present findings. Chuprina *et al.* [7] found a range of activation energies for various heat-treatment temperatures with a transition from low-temperature (600–700°C) oxidation (43 kcal/mol) to high-temperature (700–1000°C) oxidation (72 kcal/mol), which are also consistent with the present data.

Corrosion

The corrosion behavior of these oxidized wires was investigated in a companion study [20]. It was shown that the corrosion resistance is a strong function of oxide thickness where samples with the thinner (<0.1μm), more pure oxides have higher corrosion resistance. It is further illustrated that the Ni-rich regions in the thicker, less pure oxides promote localized corrosion (pitting).
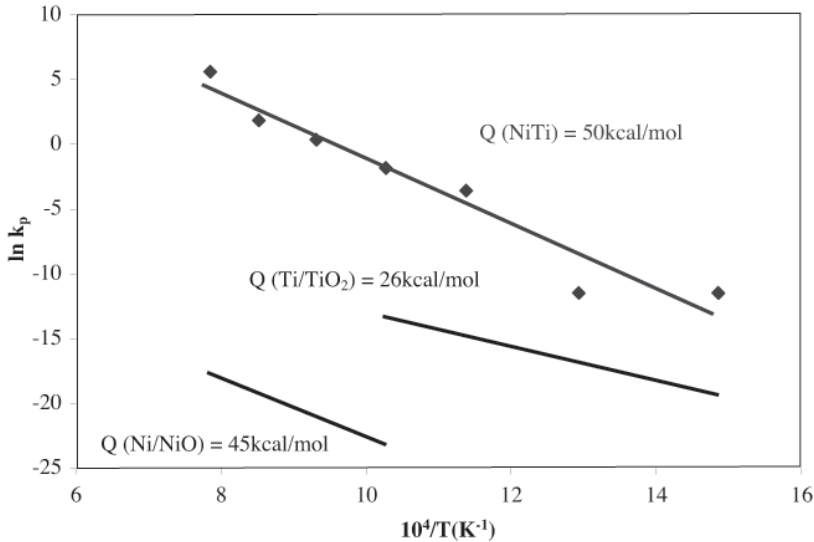
Figure 8 Arrhenius comparison of the oxidation rates for NiTi and Ti in TiO$_2$ and Ni in NiO [19].

CONCLUSIONS

The present paper shows the phase formation and kinetics of transformations for oxidized NiTi. Electropolished wires are characterized by a thin (~0.01 μm) TiO$_2$ layer. The thickness of the oxide layer increases with increasing oxidation time at temperature between 400°C and 1000°C. A Ni-rich layer is observed at the interface between NiTi and the thermal TiO$_2$. Above 800°C the Ni$_3$Ti interfacial layer transforms into Ni$_4$Ti with fingerlike projections (approximately 80at.%Ni) and Ni islands (approximately 98at.%Ni) surrounded by TiO$_2$. The oxidation reactions for these samples appear to proceed as follows:

$$NiTi + O_2 \rightarrow Ni_3Ti + TiO_2 \rightarrow Ni_4Ti + TiO_2 \rightarrow Ni + TiO_2$$
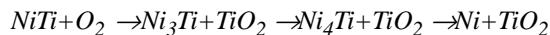
This oxide growth was determined to be parabolic, with a resultant activation energy of 50 kcal/mol. The parabolic nature of this oxide prevents further high-rate oxidation. The corrosion behavior of NiTi is highly dependent on the thickness and composition of these oxide layers.

REFERENCES

1. T. Duerig, A.R. Pelton, and D. Stoeckel, *Mater Sci Eng* **A273-275** (1999), p. 149–160.

2. D. Stoeckel, *Min. Invas. Ther. & Allied Technol.* **9** (2) (2000), p. 81–88.

3. D.E. Hodgson, M.H. Wu, and R.J. Biermann, in *ASM Metals Handbook ASM*, 10th Ed., Vol. 2 (1991), p. 897–902.

4. J. Ryhanen, in *Min. Invas. Ther. & Allied Technol.* **9** (2) (2000), p. 99–106.

5. C. Trepanier, R. Venugopalan, and A.R. Pelton, in *Shape Memory Implants*, ed. L. Yahia (2000), p. 35–45.

6. R. Venugopalan, and C. Trepanier, *Min. Invas. Ther. & Allied Technol.* **9** (2) (2000), p. 67–-74.

7. V.G. Chuprina, *Soviet Powder Metallurgy and Metal Ceramics* **28** (4) (1989), p. 468–472.

8. J.P. Espinos, A. Fernandez, and A.R. Gonzalez-Elipe, *Surf. Sci.* **295** (1993), p. 402–410.

9. R.G. Vichev *et al.*, *Proceedings of the Seventh European Conference on Applications of Surface and Interface Analysis*, eds. I. Olefjord, L. Nyborg, and D. Briggs (Goteborg) (1997), p. 679–682.

10. C. Trepanier *et al., J. Biomed. Mater. Res. (Appl. Biomater.)* **43** (1998), p. 433–440.

11. S. Trigwell *et al.*, *Sufr. Interface. Anal.* **26** (1998), p. 483–489.

12. B.L. Pelton and J. Vitarelli, in *SMST-2000: Proceedings from the International Conference on Shape Memory and Superelastic Technologies*, eds. S.M Russell and A.R. Pelton (Pacific Grove, Calif.: International Organization on SMST), p. 97–102.

13. G.S. Firstov *et al.*, *Biomaterials* **22** (2002), p. 4863–4871.

14. C.L. Chu, S.K. Wu, and Y.C. Yen, *Materials Science and Engineering* **A216** (1996), p. 193–200.

15. A.S. Khanna, *High Temperature Oxidation and Corrosion* (ASM International, 2002).

16. C.L. Zeng, *Oxidation of Metals* **58**, no.1–2 (2002), p. 171–184.

17. D.R. Gaskell, *Introduction to Metallurgical Thermodynamics*, 2nd Ed. (1981), p. 287.

18. V.G. Chuprina, *Soviet Powder Metallurgy and Metal Ceramics* **28**, no. 4 (1989), p. 310–314.

19. O. Kubaschewski and B.E. Hopkins, *Oxidation of Metals and Alloys*, 2nd Ed. (1962).

20. C. Trepanier *et al.* in *SMST-2003: Proceedings of the International Conference on Shape Memory and Superelastic Technologies*, eds. A.R. Pelton and T. Duerig (Pacific Grove, Calif.: SMST Society), these proceedings.

CORROSION RESISTANCE OF OXIDIZED NITINOL

Christine Trépanier, Lucy Zhu, Jennifer Fino and Alan R. Pelton

Nitinol Devices & Components, 47533 Westinghouse Drive, Fremont, CA 94539

ABSTRACT

In the first part of this study, we showed that electropolished NiTi wires oxidized between 400°C and 1000°C form surface layers of mixed Ni_3Ti, Ni_4Ti, Ni, and TiO_2 phases. The present study investigates by potentiodynamic polarization tests the corrosion behavior of these oxidized wires with respect to the breakdown potential (E_{bd}). The E_{bd} dramatically decreases from 1000mV to below –100mV vs. SCE as the oxide thickness increases from less than 0.01μm to 10μm. Above 10μm, however, the oxide forms a protective barrier and the E_{bd} increases to 1000mV. Samples that had been deformed by up to 3% strain in bending developed cracks in the protective titanium layer and exposed the Ni-rich phases with a concomitant decrease in E_{bd} to below –100mV vs. SCE. These results will be discussed in terms of processing parameters for medical devices.

KEYWORDS

Corrosion, Oxidation, Strain, Nitinol, Polarization

INTRODUCTION

Nitinol is rapidly becoming the material of choice for several implant devices that rely on the superelastic properties of the material, such as self-expanding stents. Although several studies have demonstrated the good corrosion resistance and biocompatibility of Nitinol [1–3], recent studies have shown that in some cases Nitinol implants can corrode *in vivo* and release high nickel content [4, 5]. It has been shown that Nitinol corrosion resistance can be significantly improved by surface treatments such as electropolishing [1]. Electropolishing of Nitinol forms a protective uniform titanium oxide layer that protects the base material from corrosion. Still, since several Nitinol implants undergo several heat treatments to shape-set the devices or adjust transformation temperatures as

the final surface treatments, it's also important to assess the effect of Nitinol oxidation on its corrosion resistance.

Therefore, the goal of this study was to determine the effect of Nitinol oxidation on its corrosion resistance. Furthermore, since most implants are used under stress-strain conditions, the influence of strain on the corrosion resistance of oxidized Nitinol will also be assessed.

EXPERIMENTAL

Materials

Nitinol wire (50.8 at.%Ni) was fully annealed at 1000°C for 30 minutes, then centerless ground to remove the oxide that formed during the full anneal. Then, the wire was electropolished to achieve a passive titanium oxide layer before subsequent oxidation treatments in an air furnace at 400–1000°C in 100°C increments and at 3, 10, 30, 100, and 300 min.

Straight and bent (3% strain) wires were used to determine the corrosion resistance of the material. To simulate shape memory application, the wires were deformed to 3% strain in bending at a temperature below their martensitic transformation temperature and then allowed to recover at room temperature.

Corrosion Testing

In accordance with ASTM F2129, an EG&G Princeton Applied Research potentiostat model 273A was used to conduct the potentiodynamic polarization corrosion tests [6]. The potentiostat was controlled by a computer with 352 SoftCorrIII-DC corrosion test software. A saturated calomel electrode (SCE) was used as a reference electrode for the potential. Two platinum auxiliary electrodes were used as counter electrodes. Testing was conducted in an appropriate polarization cell as recommended in ASTM F2129. The solution was first de-aerated for 30 minutes prior to immersion of the test sample and then throughout the test. Then, the Open Circuit Potential (OCP) was monitored for 1 hour. The polarization of the test specimen was then started 100 mV vs. SCE below the OCP at a voltage scan rate of 0.167 mV/sec. The tests were conducted in Hank's simulated physiological solution at an initial pH of 7.4±0.1. The solution was maintained at 37±1°C using a water bath. The corrosion resistance of the devices was characterized in terms of their breakdown potential (E_{bd}).

After testing, the samples were inspected with a JEOL JSM-5600 Scanning Electron Microscope (SEM) in both secondary electron imaging (SEI) and backscattered electrons imaging (BEI) modes. Composition of the oxide layer was analyzed by using Oxford Instruments Model 6587 Energy Dispersive X-Ray Spectroscopy (EDXS).

RESULTS AND DISCUSSION

Based on their breakdown potential, the corrosion resistance of the oxidized Nitinol specimens depended on the type of heat treatment (Figure 1 and Table 1). While some specimens did not show any localized corrosion, such as the electropolished sample, some specimens showed breakdown potentials as low as –140 mV vs. SCE (specimens heat treated at 500°C for 30 min.). Figure 2 illustrates the variation of the breakdown potential as a function of the oxide layer thickness (thickness of the oxide layer was assessed on heat treated specimens [7]).

As can be observed from Figure 2, there was a correlation between the breakdown potential and the oxide layer thickness. For oxide layer thickness between 0.01 and 0.05μm, the breakdown
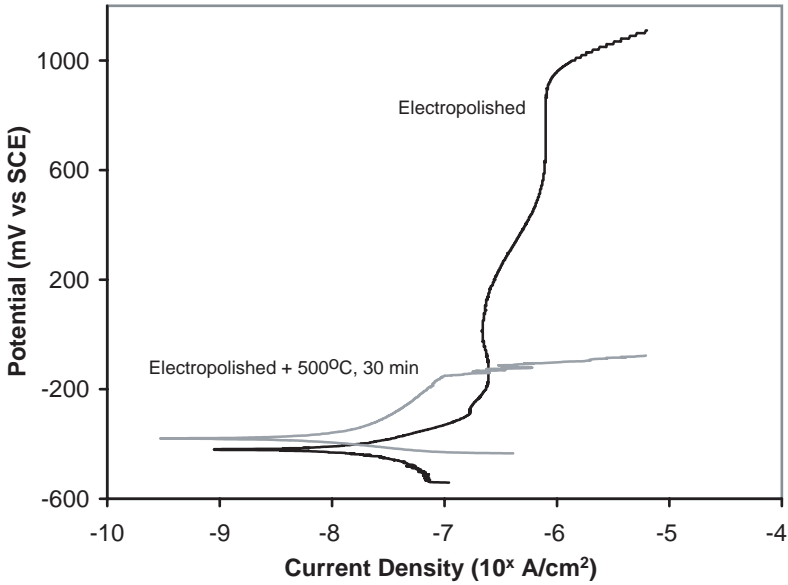
Figure 1 Polarization curves for electropolished and heat treated (500° C for 30 min.) specimens.
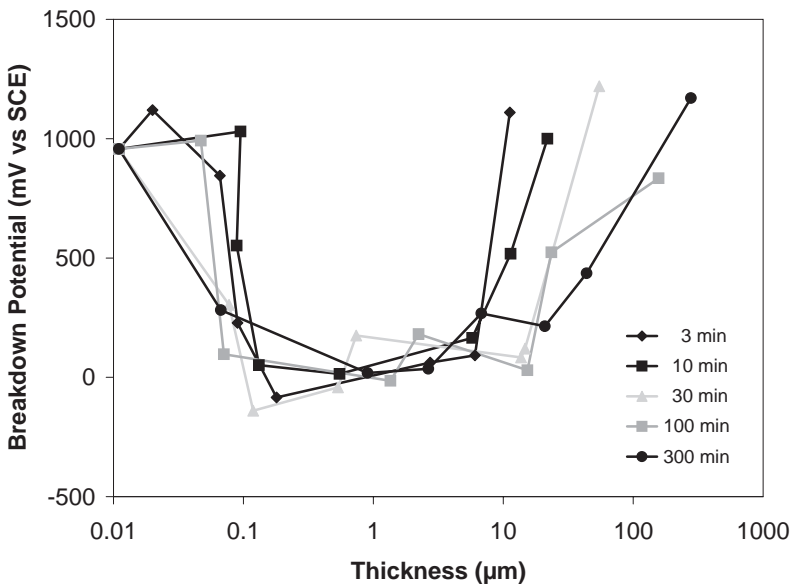
Figure 2 Breakdown potential as a function of oxide layer thickness.

potentials remained very high. Then, there was a sharp decrease in the breakdown potential starting from 0.1μm to 10μm thick oxide layer. An increase in the breakdown potential was observed for specimens with an oxide layer thicker than 10μm. It is important to note that with such a thick oxide layer, the material was insulated from the test solution.

Table 1 Breakdown Potential as Function of Heat Treatment Time and Temperature[a]

Time Temp.	3 min.	10 min.	30 min.	100 min.	300 min.
400° C	1120	1030	304	992	282
500° C	845	552	−140	97	18
600° C	228	51	−42	−14	36
700° C	−84	14	175	181	268
800° C	62	165	83	30	214
900° C	92	518	120	524	436
1000° C	1110	1000	1220	834	1170

a. Electropolished specimen's breakdown potential is 957 mV vs. SCE.

Deformation of the specimen (3% strain in bending) resulted in severe cracking of the oxide layer for specimens with a very thick oxide layer, which also greatly influenced the corrosion test results (Figure 3 and Table 2). As an example, the breakdown potential of the Nitinol specimens heat treated at 400° C for 10 min. decreased from 1030 mV vs. SCE to 417 mV vs. SCE. In general, a significant decrease in the breakdown potential was observed for the majority of the specimens (Figures 3 and 4).
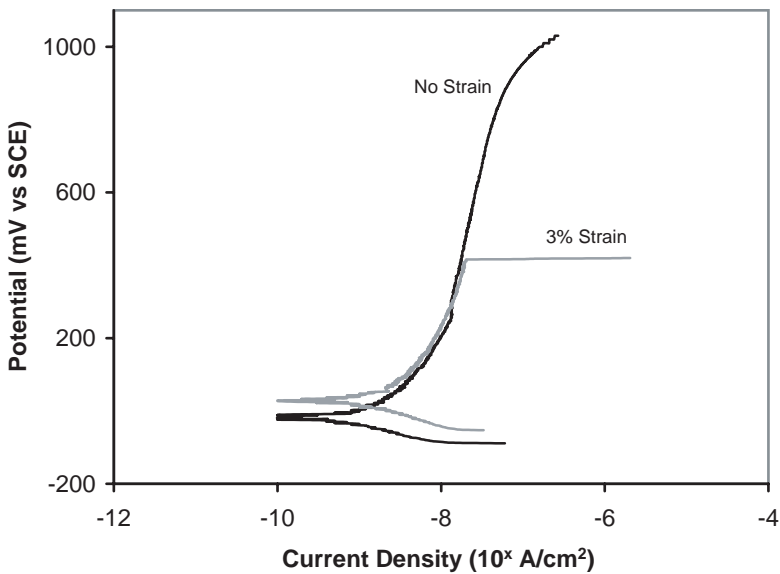
Figure 3 Effect of strain on Nitinol heat treated at 400° C for 10 min.
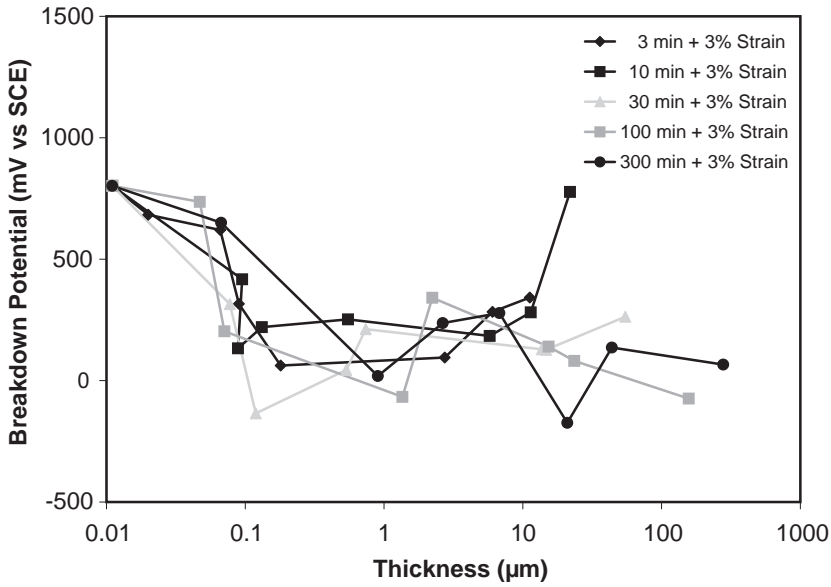
Figure 4 Breakdown potential as a function of oxide layer thickness after 3% strain.

Table 2 Breakdown potential as a function of heat treatment time and temperature after 3% strain[a]

Time Temp.	3 min.	10 min.	30 min.	100 min.	300 min.
400° C	683	417	315	736	650
500° C	620	133	−135	203	19
600° C	316	220	44	−67	237
700° C	62	252	212	341	278
800° C	95	184	129	140	−174
900° C	283	281	127	81	136
1000° C	342	777	263	−74	66

a. Electropolished specimen's breakdown potential is 802 mV vs. SCE after 3% strain.

In the first part of this study, Zhu *et al*. explored the kinetics and phase transformations of oxide formation in NiTi [7]. Using the same material and heat treatments time and temperature as was used in this study, it was observed that the oxidation appears to follow a chain of reactions as follows:

$$NiTi + O_2 \rightarrow Ni_3Ti + TiO_2 \rightarrow Ni_4Ti + TiO_2 \rightarrow Ni + TiO_2$$
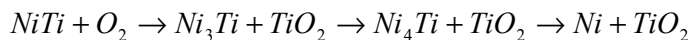
The presence, amount, and distribution of these phases depend on time and temperature. Since nickel and nickel compounds have poor corrosion resistance, the presence of nickel-rich phases in the oxide layer in Nitinol can be detrimental to the corrosion resistance of the material if exposed to the environment. It is likely that the significant decrease in the corrosion resistance of the specimens with an oxide layer thicker than 0.1μm is due to defects or breaks in the protective titanium oxide layer that was illustrated by Zhu [7]. Deformation of the specimens up to 3% strain had a similar effect. These observations are in agreement with the results from our visual inspection of the wires after corrosion testing. SEM and EDXS analyses clearly showed that localized corrosion (pitting) initiated in the Ni-rich phase (Figure 5), where the nickel-rich phase appears light gray and the titanium oxide layer appears darker gray.
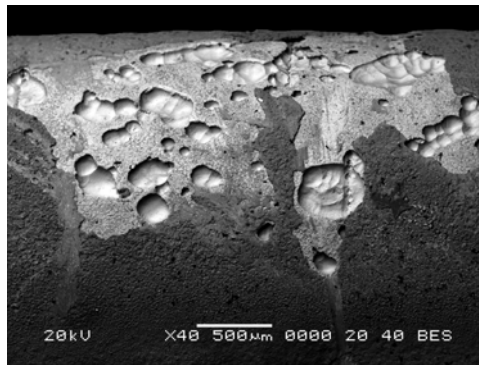
Figure 5 Pit initiation site on $1000^{o}C$, 300 min. specimen (3% strain).

These results are consistent with the results from a previous study conducted on oxidized Nitinol which showed that the uniformity and composition of the oxide layer are the determinant factors in the corrosion resistance of Nitinol [1].

Furthermore, because of its superelastic properties, it is likely that Nitinol implants will undergo significant deformation during their use. For example, the physiological strain range for implanted Nitinol stents is about 1–2% [8]. It is also not unusual for self-expandable Nitinol stents to be deformed up to 8% strain when constrained in the delivery system before their deployment. As was shown in the present study, when oxidized Nitinol is deformed, the oxide layer might crack and expose the nickel-rich phases, which can significantly lower the corrosion resistance of the material. Since the oxide layer on Nitinol is not superelastic, a thin oxide layer is preferable since it can flex and sustain the large deformations of the underlying Nitinol material without cracking.

Finally, based on these results, if Nitinol implants go through several heat treatments to shape-set or adjust the transformation temperatures of the devices, it is preferable that the implants undergo a final surface treatment to remove the thick oxide layer and passivate the surface. Furthermore, it is important to point out that unlike thermally-grown oxide that promotes the growth of mixed titanium oxide and nickel-rich phases, chemically and electrochemically grown oxide promotes pure titanium oxide formation. During chemical polishing and electropolishing, process nickel is preferentially removed.

CONCLUSIONS

This study investigated the effects of oxidized Nitinol on the corrosion resistance of the material. Our results show that

- The breakdown potential dramatically decreases from 1000mV to below –100mV vs SCE as the oxide thickness increases from less than 0.01μm to 10μm. It is likely that the significant decrease in corrosion resistance of specimens with an oxide layer thicker than 0.1μm is due to defects or breaks in the protective titanium oxide layer. These superficial cracks expose Ni-rich phases that grow during the oxidation of Nitinol. Above 10μm, however, the oxide forms a protective insulating barrier and the breakdown potential increases to 1000mV vs SCE.
- Samples deformed up to 3% strain in bending developed cracks in the protective titanium oxide layer and exposed the Ni-rich phases with a concomitant decrease in breakdown potential to below –100mV vs SCE.

REFERENCES

1. C. Trépanier, M. Tabrizian, L.H. Yahia, L. Bilodeau, and D.L. Piron, *J Biomed Mat Res* **43** *(Appl Biomater.,* 1998), p. 433.

2. R. Venugopalan and C. Trépanier, *Min Invas ther & Allied Technol* **9** (2) (2000), p. 67.

3. J. Ryhänen, *Min Invas ther & Allied Technol* **9** (2) (2000), p. 99.

4. G Riepe, C. Heintz, E. Kaiser, N. Chakfé, M.Morlock, M. Delling, and H. Imig, *Eur J Vasc Endovasc Surg* **24** (2002), p. 117.

5. A. Gimenez-Arnau, V. Riambau, E. Serra-Baldrich, and J.G. Camarasa, *Contact Dermatitis* **43** (1) (2000), p. 35.

6. F2129-01, *Annual Books of ASTM Standards, Medical Devices and Services* **13.01** (2001).

7. L. Zhu, J. Fino, and A.R. Pelton, in *SMST-2003: Proceedings of the International Conference on Shape Memory and Superelastic Technologies* (Pacific Grove, Calif.: International Organization of SMST, 2003, in press).

8. T. Lopes, X. Gong, and C. Trépanier, in *SMST-2003: Proceedings of the International Conference on Shape Memory and Superelastic Technologies* (Pacific Grove, Calif.: International Organization of SMST, 2003, in press).

EFFECT OF STRAIN ON THE CORROSION RESISTANCE OF NITINOL AND STAINLESS STEEL IN SIMULATED PHYSIOLOGICAL ENVIRONMENT

Christine Trépanier and Alan R. Pelton

Nitinol Devices and Components, 47533 Westinghouse Drive, Fremont, CA 94539

ABSTRACT

Electropolished SE-508 NiTi and passivated 316L stainless steel wires were deformed from 0% to 10% strain and were then corrosion tested in Hank's physiological solution. Results show that the breakdown potential and repassivation potential of NiTi were not affected by the strain. The breakdown and repassivation potentials were approximately 1080 mV vs. SCE and 980 mV vs. SCE, respectively for the Nitinol samples, independent of strain levels. However, the breakdown potential for the stainless steel wires decreased significantly as a function of strain. The breakdown potentials ranged from 770 mV vs. SCE for unstrained samples to 510 mV vs. SCE for the 10% strain specimens. Stainless steel specimens strained up to 8% exhibited a repassivation potential of approximately 70 mV vs. SCE. Stainless steel samples that were deformed to 10% strain did not show any repassivation potential during the reverse scan of the polarization test. Localized corrosion (pitting) initiated at the maximum strain area (in tension) on the stainless steel specimens.

KEYWORDS

Corrosion, Nitinol, Stainless steel, Strain, Polarization

INTRODUCTION

Like many biomaterials, Nitinol and stainless steel rely on a passive oxide layer to protect them against corrosion degradation *in vivo*. This oxide layer acts as a barrier against the immediate physiological environment and can prevent excessive uniform and localized corrosion from occurring. Both Nitinol and stainless steel corrosion behavior can be significantly improved by specific surface treatments such as electropolishing or passivation in an acid solution [1–3]. These passivation treatments homogenize the thickness topography and composition of the surface layer by forming passive oxide layers, predominantly titanium oxide on Nitinol and chromium oxide on stainless

steel. Previous *in vitro* corrosion studies have shown that uniformity and composition of the passive oxide layer play major roles in the corrosion resistance of these materials [1, 2].

Still, although most implants are used under stress-strain conditions, which can affect the surface properties of the oxide layer of these materials, very few corrosion studies have investigated the specific effects of stress-strain on the corrosion resistance of metallic biomaterials. Furthermore, in the case of austenitic Nitinol, a stress-induced martensite phase can be formed starting at approximately 1–2% strain. Very few studies have explored how this phase change will affect the corrosion behavior of the material.

Therefore, the goal of this study is to assess the influence of strain on the corrosion resistance of passivated Nitinol and stainless steel implant materials.

EXPERIMENTAL

Materials

Nitinol (50.8 at.%Ni) wire (NDC, Fremont, CA) and 316L stainless steel wire (Fort Wayne Metals, Fort Wayne, IN) were used in this study. Before corrosion testing, both materials were passivated to obtain surface properties similar to implant devices. The Nitinol wire was straightened and electropolished before the experiments. In accordance with ASTM F86 standard, prior to testing, the stainless steel wire was in the cold-worked condition and was passivated in a 30% nitric acid solution for 30 minutes [3]. The wires were deformed in bending so as to obtain approximately four, eight, and 10% strain, which roughly corresponds to the middle and end of the superelastic plateau, and deformation of the martensite respectively for Nitinol. Straight wire was used to determine the corrosion resistance of unstrained Nitinol.

Corrosion Testing

In accordance with ASTM F2129-01, an EG&G Princeton Applied Research potentiostat model 273A was used to conduct the potentiodynamic polarization corrosion test. The potentiostat was controlled by a computer with 352 SoftCorrIII-DC corrosion test software [4]. A saturated calomel electrode (SCE) was used as a reference electrode for the potential. Two platinum auxiliary electrodes were used as counter electrodes. Testing was conducted in an appropriate polarization cell as recommended in ASTM F2129. The solution was first de-aerated for 30 minutes prior to immersion of the test sample and also throughout the test. Then, the Open Circuit Potential (OCP) was monitored for 1 hour. The polarization of the test specimen was then started 100 mV vs. SCE below the OCP at a voltage scan rate of 0.167 mV/sec. The potential scan was reversed once the potential reached a current density value that was approximately two decades higher than the current density at the onset of the breakdown potential. The tests were conducted in Hank's simulated physiological solution at an initial pH of 7.4±0.1. The solution was maintained at 37±1°C using a water bath. Three samples were tested for each material and strain level. The corrosion resistance of the devices was characterized in terms of their corrosion potential (E_{corr}), corrosion current density (I_{corr}) breakdown potential (E_{bd}) and repassivation potential (E_p).

After testing, the samples were inspected by optical microscopy and scanning electron microscopy (SEM) (JEOL JSM-5600) to determine pit initiation sites on the wires.

RESULTS AND DISCUSSION

Typical polarization curves for each material at different strain levels are presented in Figure 1 and Figure 2 below.
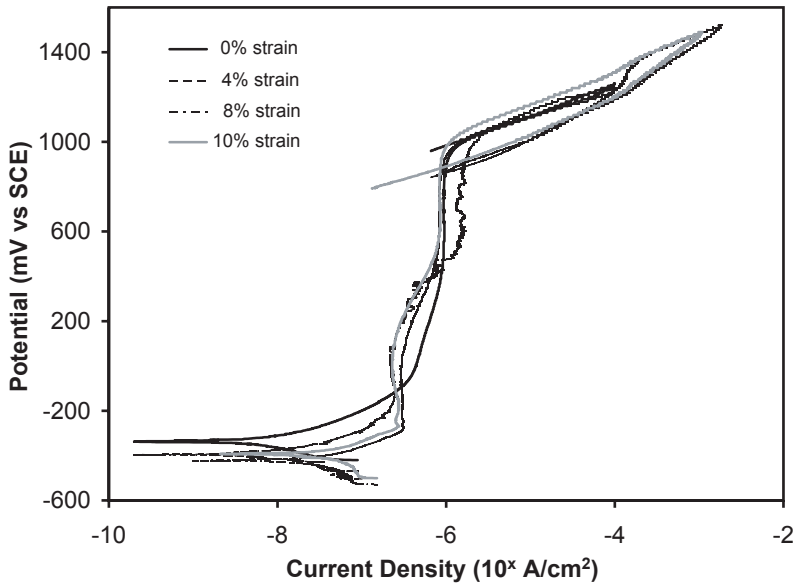

Figure 1 Polarization curves for Nitinol subjected to different strain levels.
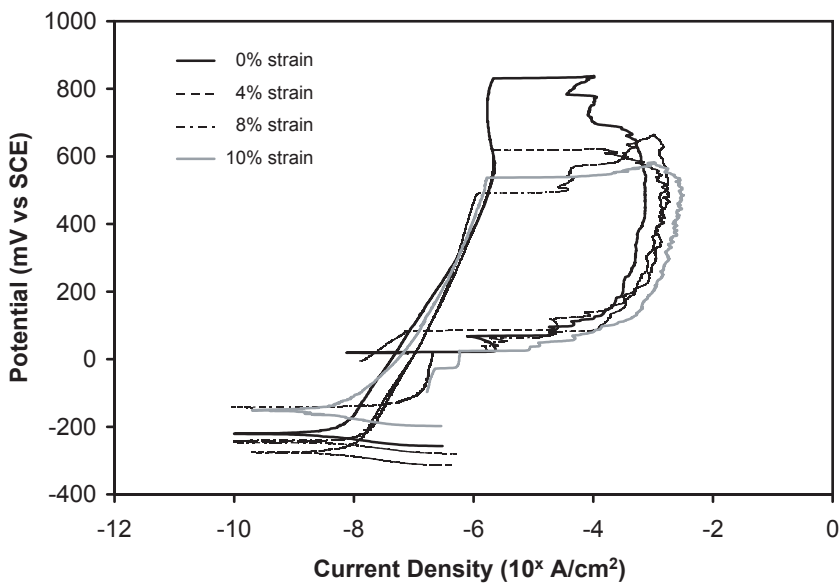

Figure 2 Polarization curves for stainless steel subjected to different strain levels.

As seen in Figure 1, Nitinol polarization curves were not significantly influenced by strain (see Figure 1). The passive region of the material remained practically unchanged for specimens deformed up to 10% bending strain. It is also important to note that Nitinol's excellent and uniform corrosion resistance is due to the electropolished oxide layer.

However, stainless steel's corrosion resistance was affected by strain (see Figure 2). Although its passive region was not significantly changed, the breakdown potential of the material was shifted to lower values.

The influence of applied strain on the corrosion test results for the Nitinol and stainless steel wires are summarized in Table 1 and Table 2, respectively.

Table 1 Corrosion Test Results for Nitinol Wire at Different Strain Levels (mean ±SD)

Bending strain %	E_{corr} mV vs. SCE	I_{corr} nA/cm^2	E_{bd} mV vs. SCE	E_p mV vs. SCE
0	−323±31	10±4	1143±73	1063±45
4	−408±29	25±11	1030±79	948±46
8	−462±35	46±11	1174±194	1059±237
10	−400±7	21±129	993±23	865±14

Table 2 Corrosion Test Results for Stainless Steel Wire at Different Strain Levels (mean ±SD)

Bending strain %	E_{corr} mV vs. SCE	I_{corr} nA/cm^2	E_{bd} mV vs. SCE	E_p mV vs. SCE
0	−215±76	3±1	769±65	68±46
4	−152±109	3±0	556±52	104±29
8	−188±78	4±3	515±32	36±149
10	−110±7	4±1	510±25	N/A[a]

a. Specimens did not repassivate.

Based on the results reported in Table 1, none of the corrosion parameters (E_{corr}, I_{corr}, E_{bd}, and E_p) were significantly affected by an increase in the strain for Nitinol. Although the breakdown (E_{bd}) and repassivation potentials (E_p) seemed lower for the specimens strained up to 10%, none of the samples reached the breakdown of the oxide layer (pitting). These results were in accordance with a previous study conducted by Rondelli, who found that the breakdown potential of Nitinol specimens strained up to 4% in tension was not significantly affected [5].

Furthermore, these results indicate that the presence of stress-induced martensite in Nitinol does not significantly affect its corrosion resistance. Therefore, the uniformity and composition of the

passive oxide layer, as opposed to the crystallographic phase, appeared to be the predominant factors in the corrosion behavior of Nitinol.

Stainless steel's corrosion potential (E_{corr}) and corrosion current density (I_{corr}) values were not significantly affected by an increased in strain (ref. Table 2). However, stainless steel's breakdown potential significantly decreased after applying 4% bending strain ($p<0.05$, Student T-test). Indeed, stainless steel breakdown potential decreased from 769 mV vs. SCE to 556 mV vs. SCE after 4% strain. Strain increase from 4% to 10% did not further affect the breakdown potential ($p>0.05$, Student t-test). For bending strains up to 8%, no significant effects were observed for stainless steel repassivation potential, in part because of the large variability in this parameter. However, the specimens that were bent up to 10% did not repassivate upon reversal of the potential scan. These results are in accordance with a study from Bundy et al., who found that 316L stainless steel's breakdown potential was significantly decreased after application of stress [6].

Visual inspection of the stainless steel test specimens after the corrosion test revealed that localized corrosion (pitting) had initiated at the maximum strain area (in tension) on the wires. Furthermore, superficial cracking of the oxide layer was observed in the same area (see Figure 3). No indication of localized corrosion was observed on the Nitinol wires. The surface of the Nitinol wires remained smooth and uniform even after 10% strain (see Figure 3). This result highlighted the benefits of a thin electropolished layer, which was able to sustain large deformation without cracking or peeling and therefore offers superior protection against corrosion. In another study, we showed that bending of heat treated Nitinol wires, which exhibited a thicker oxide layer, disrupted the protective oxide layer and led to a significant decrease in the corrosion resistance of the material [7].
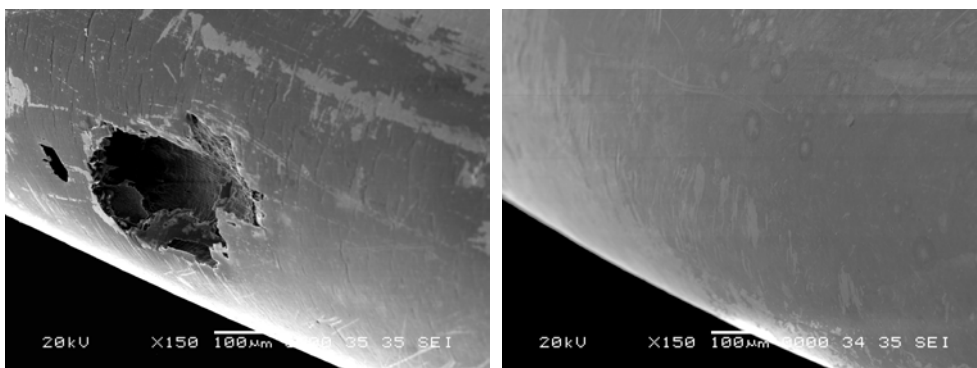
Figure 3 (left) Pit initiation site on stainless steel wire (10% strain) (right) Nitinol wire postcorrosion testing (10% strain).

These results emphasize the importance of the uniformity of the oxide layer to protect stainless steel and Nitinol against corrosion. Furthermore, disruption of the passive film during deformation and slow repassivation kinetics appear to be the underlying mechanisms of the decrease in the corrosion resistance of stainless steel.

Generally, the applied strains in this study were higher than the normal expected range for implant devices. For example, stainless steel balloon-expandable stents are usually designed to reach more than 25% strain during deployment [8]. However, the physiological strain range for implanted Nitinol stents is about 1–2% strain [9]. It is also not unusual for self-expandable Nitinol stents to be deformed up to 8% strain when constrained in the delivery system before deployment. Higher strain

levels were investigated in this study to investigate Nitinol's full superelastic plateau and determine if strain-induced corrosion effects would be observable.

CONCLUSIONS

This study investigated the influence of strain on the corrosion resistance of passivated Nitinol and stainless steel implant materials. Our results show that

- Nitinol's corrosion resistance was not affected by strains up to 10%. Indeed, the uniformity of the protective titanium oxide layer on the electropolished Nitinol was not compromised by the deformation.
- The presence of stress-induced martensite did not affect Nitinol's corrosion resistance. The composition and uniformity of the passive titanium oxide layer appear to be the predominant factor in the corrosion resistance of the material, independent of the underlying crystallographic phase.
- Stainless steel's resistance to localized corrosion was affected by strain. Disruption of the passive film during deformation and slow repassivation kinetics appear to be the underlying mechanisms of the decrease in the corrosion resistance of stainless steel.

REFERENCES

1. C. Trépanier, M. Tabrizian, L'H. Yahia, L. Bilodeau, and D.L. Piron, *J Biomed Mat Res* **43** (Appl Biomater, 1998), p. 433.

2. R. Venugopalan and C. Trépanier, *Min. Invas. Ther. & Allied Technol.* **9** (2) (2000), p. 67.

3. F86–91, in *Annual Books of ASTM Standards, Medical Devices and Services* **13.01** (1991).

4. F2129-01, in *Annual Books of ASTM Standards, Medical Devices and Services* **13.01** (2001).

5. G. Rondelli and B. Vicentini, *J Biomed Mater Res* **51** (2000), p. 47.

6. K.J. Bundy, C.J. Williams, and R.E. Luedemann, *Biomaterials* **12** (1991), p. 627.

7. C. Trépanier, L. Zhu, J. Fino, and A.R. Pelton, in *SMST-2003: Proceedings of the International Conference on Shape Memory and Superelastic Technologies* (Pacific Grove, Calif.: International Organization on SMST, 2003, in press).

8. Seik Oh, in *ABAQUS Users' Conference* (Newport, Rhode Island, 2000), p. 535.

9. T. Lopes, X. Gong, and C. Trépanier, in *SMST-2003: Proceedings of the International Conference on Shape Memory and Superelastic Technologies* (Pacific Grove, Calif.: International Organization on SMST, 2003, these proceedings).

DESIGNING WITH NITINOL FOR THE COMMONER

K. Freislinger Luehrs

Nitinol Devices and Components, a Johnson & Johnson Company
47533 Westinghouse Drive, Fremont, CA 94539

ABSTRACT

There are two ways that Nitinol gets used. The first is genuine need. The application calls for constant force, or superelastic or thermal shape recovery. The second: Nitinol is cool. Where can I use it? As a designer, it is important to distinguish between novelty and genuine need. Processing and availability issues are significant. Alloying, quality, machining, heat treatment, postprocessing, and design can get complicated. Ultimately, you do not need to be a material scientist to develop a quality product. Material properties can be simplified. Processing can be researched and equipment purchased. Qualifications, analyses, and testing can be performed.

KEYWORDS

NiTi, Nitinol, Design, Cost, Finite Element Analysis, Product, Material, Manufacturing, Quality, Availability, Analysis, Prototyping, Testing, Inspection

INTRODUCTION

It happens in industry that nickel titanium is proposed for use in new device designs. When this occurs in a group or company unfamiliar with the material, significant barriers and hurdles present themselves. Although the shape memory or superelastic properties of the materials look promising, getting a handle on their limitations is critical right from the start. Prototyping and iterating can be difficult, if not impossible, without specialized equipment, confidential manufacturing information or a relationship with an existing prototype subcontractor. Precision design, utilizing Finite Element Analysis (FEA), is also more difficult than with standard materials because of the material non-linearity. Again, specialty subcontractors can help with this. Special FEA software and training are required in order to accurately perform these analyses in-house.

Even after all of this, there are major unexpected pitfalls to avoid on the way to developing a necessary and successful Nitinol product.

Raw material must be accessible and of consistent quality and processing. The price must be consistent with the intended use. Production designs must consider the device operating environment and life cycle, from shelf to disposal, and how the properties of the material may be impacted. These subject areas include, but are not limited to, strain cycling, mechanical fatigue life, surface preparations, and geometric considerations. Manufacturing limitations must be anticipated and controlled with an appropriate quality system. Significant limitations exist in machining, heat treatment, postprocessing, and assembly techniques among others. Finally, aspects such as surface quality and transition temperature require unique inspection and quality-control procedures.

INTENDED PURPOSE

The foremost question to answer is the question of motivation. Does the intended application really require the use of nickel titanium? Is it a constant force application? Is it an application requiring superelasticity or thermal shape recovery? See Figures 1 and 2. Figure 1 illustrates that effects of A_f temperature on the mechanical properties at a test temperature of $37°C$. Figure 2 schematically shows the shape memory effect in a wirelike structure. NiTi provides these properties, with limitations, when used appropriately. It is easy to slip into believing that this magical material will solve unsolvable engineering challenges. It cannot create the highly desirable catheter tubing with the ID larger than the OD. If there is a less exotic material, be it a metal, plastic or elastomer, which can provide the necessary properties, generally, it is preferable to use it.
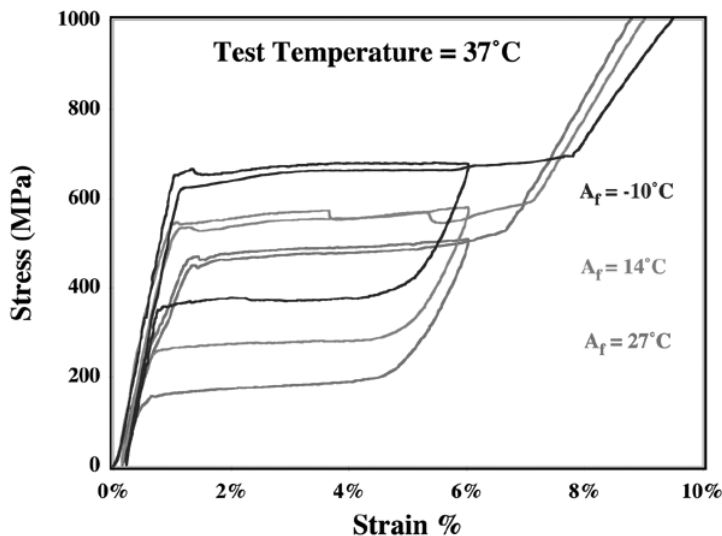
Figure 1 Sample stress vs. strain curve for various temperatures. Notice the superelasticity demonstrated between 1% and 6% strain. The sample returns to essentially zero deflection after being strained to such an extent. Also visible is the characteristic "plateau," which demonstrates the material's consistent force over a range of deflection. Nitinol's nonlinear behavior, particularly relevant in FEA, is shown, as well as the influence of temperature on material strength.

Shape Set

Deformed Cold

Return to Set Shape upon Warming
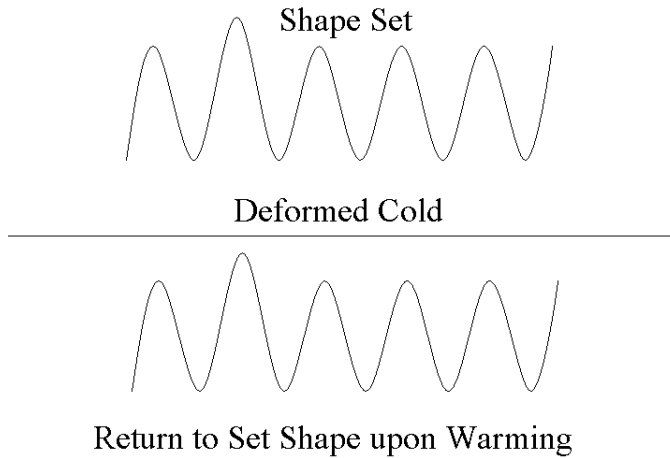
Figure 2 Pictogram of thermal shape set and recovery mechanism.

Nitinol products have historically been susceptible to use purely for the novelty of it. Although practical advantages can be imagined, many of these ideas approach science fiction. A quick Internet search provided examples including a Nitinol shirt, a penile implant and even a Nitinol impregnated bra. Also, it is hard to imagine a product for which an unnecessary nickel titanium base material would be a substantial enough selling point to outweigh the many disadvantages and complications that come along with it. The cost of these endeavors can reach the stratosphere, well beyond the reach of the intended market.

BARRIERS TO ENTRY

Most engineers who have worked with Nitinol will tell you that at one time or another they have had a hard time getting their hands on the raw material of their choice. It has been unofficially called "Un-obtainium." Although the situation has improved some recently, especially for the engineer within a Nitinol company, there are still problems getting exactly what you want. It has been relatively common practice to centerless grind tubing to get the desired dimensions. This exaggerates existing concentricity imperfections. Sheet and strip have limited availability and preprocessing and aspect ratio issues, respectively. It can be difficult, prohibitively expensive, and time consuming to obtain custom material in small quantities, potentially driving a project to failure. Beyond dimensional, there are a multitude of variables that can be specified, including: cold work, contaminants (Figure 3), primary and secondary compositions, surface texture, and more.

Cost is integral in the decision to use Nitinol in a commercial product. For common forms, Nitinol can cost 5–20 times more than stainless steel. So for a small component with a healthy sales price, the difference in material costs will have little impact. But for a product heavy in material and lower in price, the overall product cost may again be beyond the reach of the intended market.

For those of us preferring to prototype and iterate to design perfection, the specialized equipment and confidential manufacturing information necessary to make functional prototypes become significant hurdles. Even for those accustomed to computer analyses, design by FEA and computer-aided rapid prototyping techniques, nothing can capture the defining mechanical properties like the
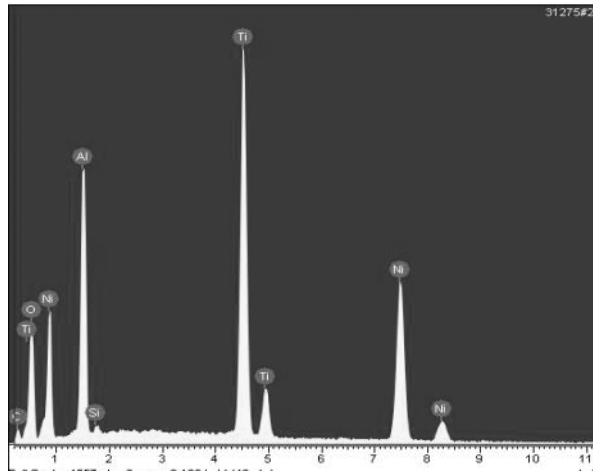
Figure 3 Sample Energy-Dispersive X-ray Spectra (EDXS) analysis reveals typical contaminants in an unidentified sample. Elements present: Titanium, Nickel, Aluminum, Oxygen, Carbon, and Silicon.

real thing. It can be like designing in the dark and designing for function without feedback. One approach might be to use a different form or scale of the right material to capture the mechanical behavior.

Any of these may be improved by working with a qualified prototype house.

DESIGN

In most respects designing with Nitinol is similar to designing with any other material. It is important to remember that the nickel titanium alloy has mechanical material property limitations. In cycling, it has a finite life, both in mechanical and strain fatigue. For example, the fatigue life of a device cycled mechanically will depend on the device dimensional design; the cyclic strain; the ambient temperature; material properties such as transition temperatures, material strength, surface characteristics; and other influences. It is also possible to strain cycle the material thermally, by cycling the ambient temperature. The alteration of these variables can produce a fatigue life anywhere between zero to millions of cycles.

Similarly, there is a limit to the amount of strain potentially recoverable. This is generally considered to be 6–8%. This is an important number to which to design, and is also relevant in establishing limits on wire bend radii. For thermal recovery applications, it is important to note that subtle changes in temperature will not be sufficient to bring a device from a fully malleable state to a fully austenitic one. This temperature range from M_f to A_f is in the order of magnitude of 30–50°C. As might be imagined, this property limits industrial and medical thermal recovery applications.

FEA is accurately performed on Nitinol designs in many companies as illustrated in several papers in these proceedings. Software specifically written to handle the nonlinear behavior is available for purchase and training is available (Figure 4). Presumably, library curves are available and, of course, your own data curves may be entered for running the analysis. Alternatively, there are consulting firms active and available in this area to perform necessary analyses.
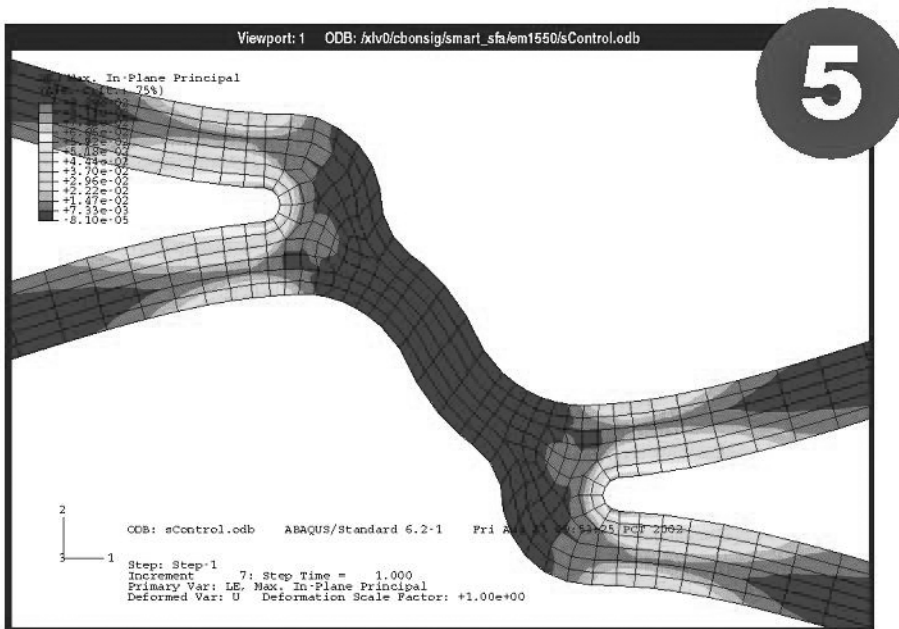
Figure 4 Sample FEA plot. A trained analyst with the appropriate software can produce accurate and predictable results.

MANUFACTURING

As mentioned, specialized equipment and significant manufacturing information is necessary to process Nitinol components. Machining might be by laser, ElectroDischarge Machining (EDM), photochemical etching, conventional machining, or other method. Heat treatments may be done in an oven furnace or salt pot, but are done at extraordinarily high temperatures, such as above 400° C. Different temperature and time combinations will produce a variety of results in a part, and selecting the optimal heat treatment would most accurately be considered part of the design process. The tooling required to shape set a part may also be complex and vital.

Post-heat treatment processing steps, such as polishing, can be critical. In some scenarios a corrosive environment can produce astonishing results (Figure 5). At this time there is no "easy" joining technology. Welding, gluing, soldering, and assembly are possible but difficult.

QUALITY CONTROL

At the end of the day, as in most manufacturing environments, it is necessary to verify and validate your designs, processes, and components. Through standard techniques, such as design of experiments and statistically supported qualifications and validations, unique processes and specifications can be controlled. Some attributes require unique and sometimes tedious inspection and test techniques. For example, Scanning Electron Microscopy (SEM) works well for establishing acceptable criteria for surface imperfections (Figure 5), although magnified visual inspection probably would be used more routinely for this purpose and to look for other geometric irregularities (Figure 6).

An additional attribute unique to Nitinol characterization is transition temperature. A complete curve, including austentitic and martinsitic transformation temperatures, may be obtained by using
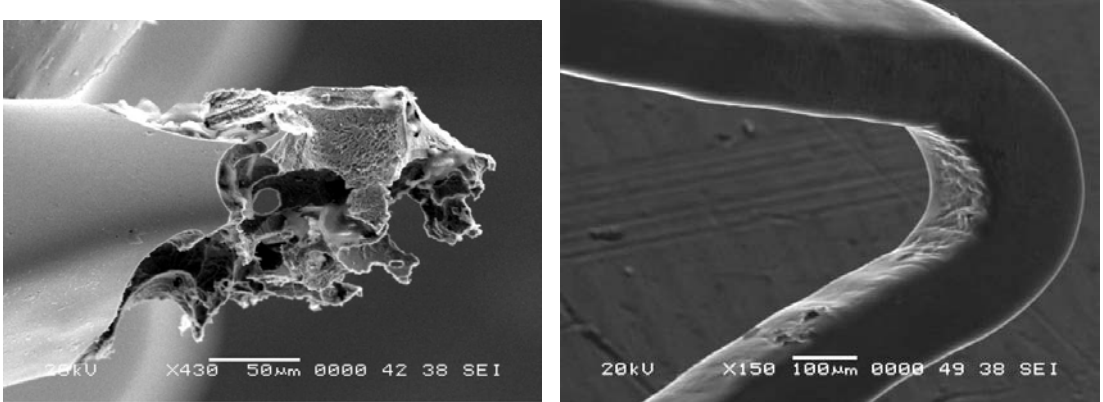
Figure 5 (left) SEM view of corrosion damage in a contrived bench top test. (right) Sample SEM evaluation of surface quality on Nitinol component.
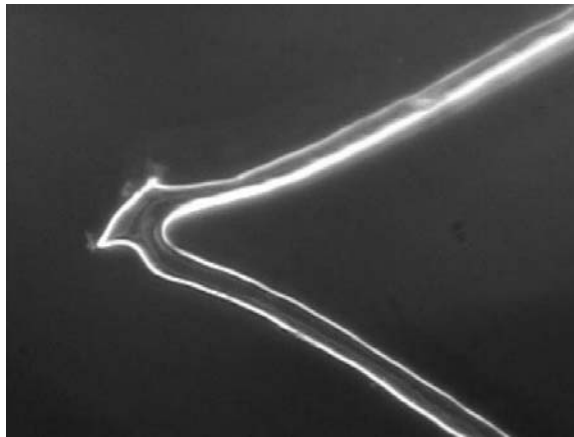
Figure 6 Sample defect found through magnified visual inspection.

a Differential Scanning Calorimetry (DSC) calorimeter (Figure 7). Alternatively, temperature vs. deflection data may be collected to establish an austenite finish (A_f) temperature. This may be in the form of a curve (Figure 8), or gauged against go-no go tooling for simplicity.

CONCLUSION

Once a device need has been properly established, Nitinol can be used effectively to create a well-designed and well-placed product. Outsourcing is a simple solution to moving past the typical barriers to entry. Solid planning and a few strategic purchases may sufficiently establish sufficient internal capability to produce a quality product. Conversely, it is critical to stay on top of potential issues and not wrap up an engineering effort too soon.

ACKNOWLEDGEMENTS
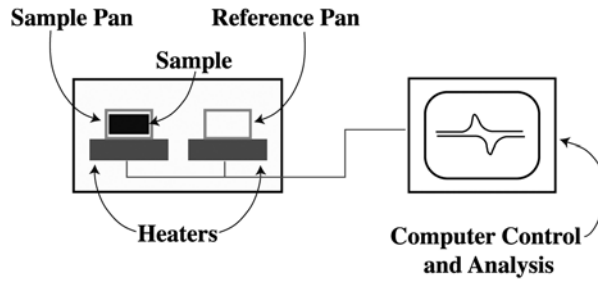
Figure 7 DSC calorimeter schematic. The DSC test provides complete transition temperature information, including austenite start and finish, as well as martensite start and finish. It is a thermal test performed on specially prepared samples. It is not appropriate for testing finished goods.

Figure 8 Sample mechanical A_f test plots dimensional changes vs. temperature to determine transition temperatures.

FINITE ELEMENT ANALYSIS ON NITINOL MEDICAL APPLICATIONS

Xiao-Yan Gong and Alan R. Pelton

Nitinol Devices & Components, 47533 Westinghouse Drive, Fremont, CA 94539

ABSTRACT

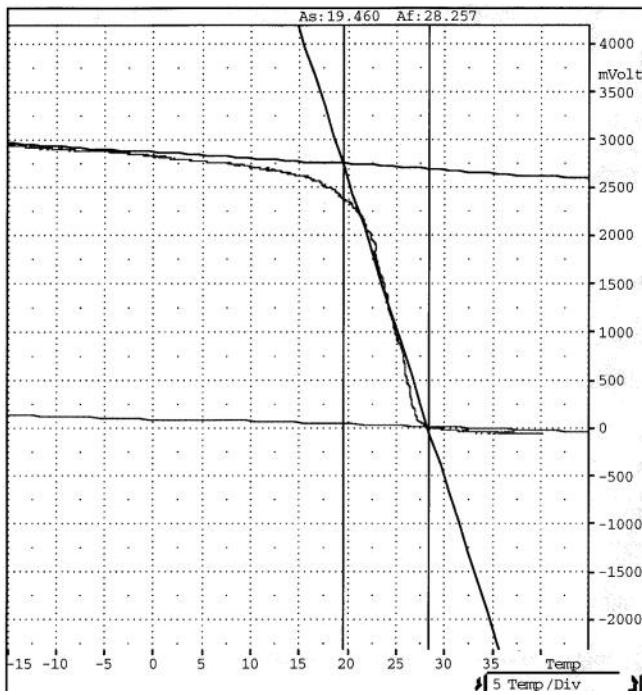This article presents two applications of nonlinear Finite Element Analysis (FEA). In the first example, FEA predicts the stress-strain response of a superelastic Nitinol device at different austenite finish temperatures (A_f) when tested at 37°C. The second example illustrates the method for evaluating a stent's fatigue performance. The analyses are found to agree well with the theoretical prediction and/or experimental measurement. The focus of this presentation is on the use of FEA as a predictive design tool for fast prototyping of Nitinol medical devices.

KEYWORDS

NiTi, Finite Element Analysis, Medical Application, Stent, Minimally Invasive Surgery

INTRODUCTION

Nitinol's biocompatibility has made it a great material for many medical applications such as dentures, orthodontic arch wires, needles, guide wires, heart valve instruments, self-expanding stents, vena cava filters, minimally invasive surgery instruments, and septal defect occlusion systems, to name a few [1–4]. Many of these devices are implanted into the human body via minimally invasive surgical procedures taking advantage of the unique superelastic behavior of Nitinol. With increasing market demand and competition, a predictive method that can shorten the time and resources from design to production becomes the key in new product development. Traditional beam theory provides reasonable estimations in some applications, but success is limited to small strain [5]. Nonlinear Finite Element Analysis (FEA), which is capable of not only dealing with the complicated geometry, but also modeling the nonlinear material response, becomes more and more important in product design.

The superelastic material behavior generates analysis difficulties due to its path-dependence and high nonlinearity. This calls for efficient constitutive modeling because it is inevitable that numerical iteration is necessary during the analysis. Phenomenological approaches are the most suitable solution for the simulation efficiency. Theories based on either the generalized plasticity theory, which focuses on the material response at a given temperature, or a free energy framework, which focuses on the temperature dependencies of the material, or even the micromechanics models have been developed independently in the past decade [6–13]. Based on several of these approaches, ABAQUS West commercialized a User-defined Material (UMAT) subroutine specific to Nitinol based on the generalized plasticity theory [7–9]. Many applications demonstrated that the UMAT is capable of predicting the uniaxial material response at different temperatures, a Nitinol stent's deformation, and Austenite or Martensite composition at any material point in addition to the stress and strain fields [14–15]. Therefore, it is used in the analyses presented in this paper. Recently, comparison of the Abaqus West UMAT and another UMAT by EchoBio has shown that both approaches agree very well with one another and they both predict the experiment results well [16].

This article focuses on analyzing Nitinol's medical applications in minimally invasive surgery. The analyses are divided into two categories. We choose a representative device from each category and discuss the analysis in detail. The first device analyzed is a Nitinol needle/wire locator. The second device is a self-expanding stent. They are chosen with general indications on many other applications as listed in the section below. In both cases, experimental data are used to compare with the analysis results. Theoretical estimations are also provided to further confirm the analysis results.

In the needle/wire locator application, we show that the UMAT is able to predict the uniaxial material response at different austenite finish temperature (A_f) by comparing with the experimental data. This opens doors for the optimization of the A_f to achieve the most suitable design. It also indicates that the material properties at different A_f or application temperatures are predictive. The stress analysis on the device is straightforward since the hook wire is constrained very tightly inside the needle. Furthermore, the peak stress and strain values can be estimated from pure geometry change. Comparison shows that FEA agrees well with the theoretical prediction.

In the stent application, we briefly review the FEA procedures in evaluating a stent's fatigue strains *in vivo*. Our focus is aimed on the FEA results on a fatigue specimen simulating the deformation of stentlike devices, i.e., a diamond-shaped specimen. Fatigue tests on this test specimen are used to set up the strain-life curve that dictates the baseline for fatigue prediction [17]. FEA results on diamond shaped specimen are compared with the load-displacement results collected from the experiment. A theoretical solution based on a piece-wise linear approximation in combination with the fundamental beam theory is generated on the loading portion of the specimen for comparison. Results show good agreement between FEA, theoretical prediction, and the experimental data.

NEEDLE/WIRE LOCATOR

Figure 1 shows the Mitek Homer Mammalok needle/wire locator. It is a two-piece device that consists of a Nitinol wire with a semicircular-shaped hook at one end, which served as a locator to identify the tumor location in the application, and a hollow needle that the wire slides into. The locator is originally withdrawn inside the needle cannula [18]. During the application, the needle is inserted into the breast and adjusted until its tip is verified to be at the site of the tumor. The locator is then advanced and reforms the hook configuration. The position of the hook marks the correct location for the surgeon. If necessary, the locator can be withdrawn into the needle until the correct location is identified.

The design challenge was to have a strong hook so that it can be placed in position tightly, yet was not too hard to withdraw into the needle. One of the possible design options, from a material application point, was to choose the right A_f temperature. Pelton et al. provided details on how to obtain the desired A_f [19]. Pelton et al. later also pointed out that the best way to optimize both A_f and the geometry is to perform FEA without actually making and testing the device [20]. This type of FEA normally involves a curved wire withdrawn into a straight tube. The analysis is very straightforward. One can mesh the wire with solid elements and simplify the needle as a rigid cylinder. Use of symmetry can reduce the model to a half of its actual size. Prescribed displacement condition can be used to pull the wire through the rigid cylinder. The outputs from FEA are the stress and strain fields and the contact pressure between the wire and the needle (rigid surface). The wire diameter is 0.38 mm and the hook radius is 4.8 mm in this study. The maximum tensile and compressive strains are theoretically estimated from the curved beam theory to be approximately 4.1% and –3.8% respectively.

A uniaxial tensile test is necessary to calibrate the UMAT for analysis. For comparison purposes, the tests were performed at 37°C for wires that are processed to have three different A_f temperatures, i.e., –10°C, 14°C and 27°C. We used the highest A_f, i.e., $A_f = 27$°C, to calibrate the UMAT. We then run a single element test to predict the stress-strain relations for the other two A_f wires. Figure 2 shows the comparison of the FEA prediction and the experimental results of the highest A_f wire. As one can tell, the calibrated material response reproduces the experimental results very well. Figure 3 shows the comparison of the FEA prediction and the experimental results on the lower A_f wires. Again, the results agree, especially well in the range of application interests, i.e., up to 6%.

Figure 1 Mitek Homer Mammalok needle/wire locator.
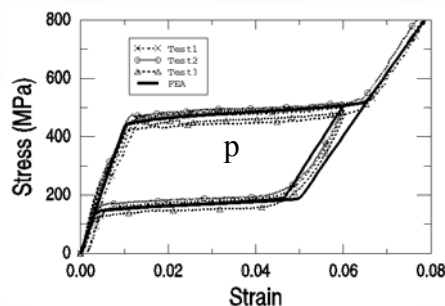
Figure 2 FEA material model calibrated using $A_f = 27$°C.

Figure 4 shows stress contour on the deformed shape for different A_f wires when they are withdrawn into the needle. Clearly the different A_f wires produce different magnitudes of stress field. The lower the A_f, the higher the stress it produces. Therefore, the lower the A_f, the harder it is to withdraw the wire into the needle. When the strain contours are plotted, there is less difference
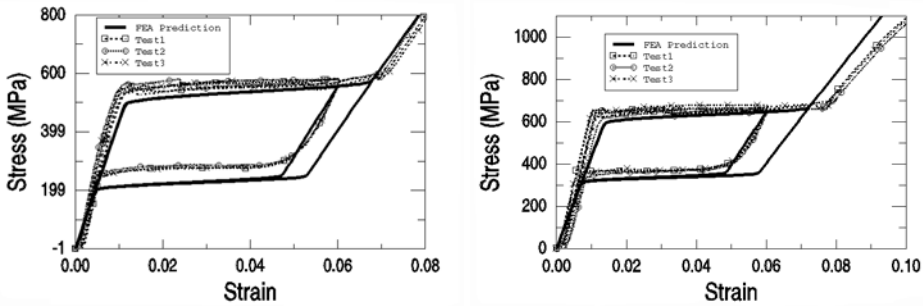
Figure 3 (left) Comparison of the uniaxial tensile tests on $A_f = 14°C$ wires with FEA prediction from the $A_f = 27°C$ input data, (right) Comparison of the uniaxial tensile tests on $A_f = -10°C$ wires with FEA prediction from the $A_f = 27°C$ input data.

between the different A_f wires. This is because the deformation is bending dominant and the wire is so well confined in the needle—despite the different material responses for the different A_f temperatures, the strain field is independent of the material response. Figure 5 plots the comparison of strain distributions for different A_f wires and the theoretical prediction based on nonlinear beam theory when the loading portion of the Nitinol's stress-strain response is approximated as piecewise linear elasticity. The results are almost identical. Notice these are the strain distributions in the body portion of the arc of the wire; at the locations where the wire changes from straight to arc the strain is slightly higher. This phenomenon, normally referred to as an end effect, can only be predicted from the FEA. Figure 5 shows the strain distribution at this location with comparison to theoretical prediction. As one can see, the strain is higher than the body portion of the curved wire. Therefore, even theory and FEA agree closely on predicting the strain in the body portion of the curved wire. FEA can also capture the end effect nicely and predict the strain more accurately.

This analysis technique also applies to other wire-shaped devices such as a duct-occlusion device, a radio frequency interstitial tissue ablation device, and a hingeless grasper [1–2] and withdrawing of a vena cava filter.

STENT FATIGUE ANALYSIS

A stent is a metal mesh made either from fine wires or from laser cutting tubes into desired patterns set in place to hold a vessel open. The superelastic behavior of Nitinol eased the design due to its large strain capability. Duerig et al. discussed the most important differences between a balloon expandable stent normally made of stainless steel and a self-expanding stent made of Nitinol in addition to the key design issues [21–22]. Regardless of their differences, the most important design issues for a successful stent remain its fatigue life and the stent stiffness. Testing of a Nitinol stent's stiffness and corresponding prediction from nonlinear FEA was straightforward. Gong et al. have demonstrated recently that FEA prediction of a Nitinol's stiffness agrees with the experiment [16].

However, prediction of a Nitinol stent's fatigue performance was not an easy task. Based on the fundamental strain-life approach, prediction of a stent's fatigue performance required a precise analysis of the fatigue strains of a stent *in vivo* and a profound understanding of Nitinol's fatigue behavior under the similar deformation patterns. Nonlinear FEA has been shown to be very effective in computing the fatigue stresses of a balloon expandable stent made of stainless steel
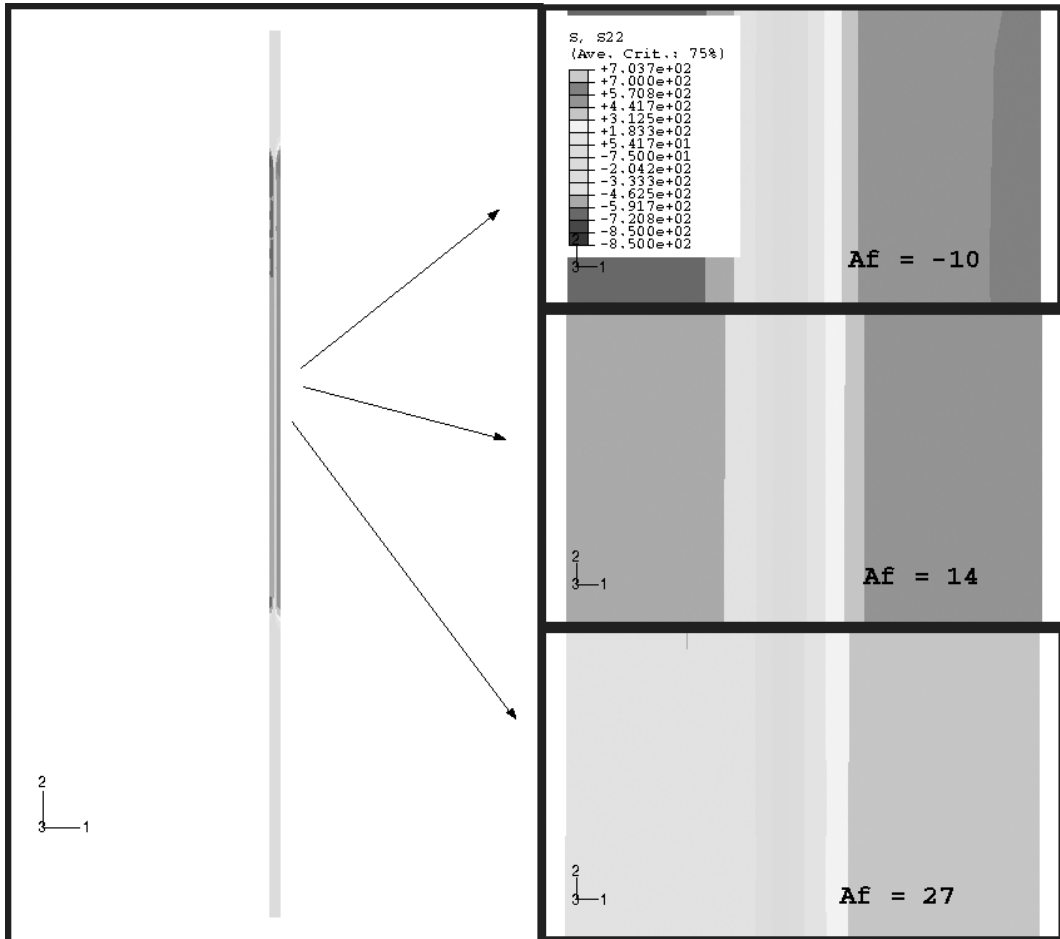
Figure 4 Longitudinal stress contours in the same scale when a different A_f Nitinol locator has been withdrawn inside the needle indicates stress increases as A_f decreases.

[23]. A similar approach applies to Nitinol self-expanding stents, yet Nitinol's complicated material properties and multiple expansion and shape set steps in stent manufacturing discouraged the fatigue analysis of the self-expanding stent's fatigue strains in a single FEA from the "as-cut" stent configuration. Therefore, we proposed to compute the Nitinol self-expanding stent's fatigue strain from its manufactured configuration. An example of an FEA model for computing the fatigue strains of a Nitinol stent *in vivo* is shown in Figure 6. The model contained a Nitinol stent and a straight artery to simulate the interaction of a stent and the artery *in vivo*. Because the fundamental fatigue data or the strain-life curve was collected on the loading portion of Nitinol's stress-strain response, it was very important that the fatigue strain was also evaluated on the loading portion of Nitinol's stress-strain response. For this reason, the fatigue strain analysis technique for a Nitinol self-expanding stent was simulated in the following two steps. The flexible contact between the artery and the stent was "turned off" until the final stage of the analysis. To ensure that the fatigue strains are evaluated at the loading path of the Nitinol, the first step of analysis was to expand the artery to a diameter that was slightly larger than the stent outer diameter (OD). This was done by

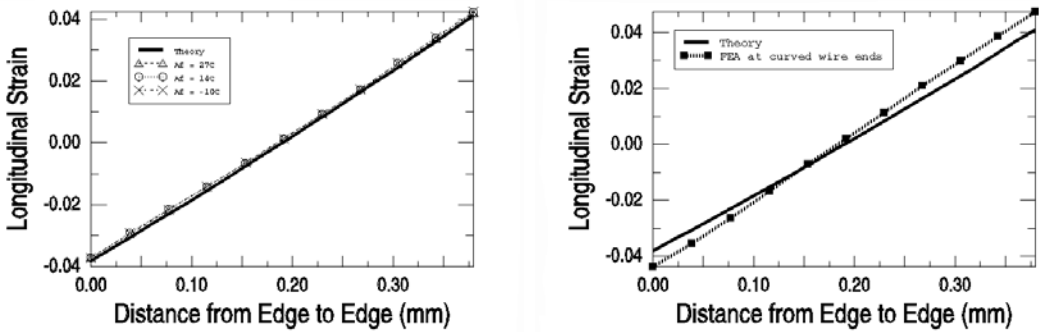*Figure 5 (left) Edge-to-edge longitudinal strain distribution when Nitinol locator was withdrawn inside the needle, (right) Edge-to-edge longitudinal strain distribution comparison at the end of a curved wire when it was withdrawn inside the needle.*

applying an internal pressure on the artery. In the second step, the contact between artery and stent was turned on and the pressure applied to the artery in the first step was now ramped down to zero. As the pressure was ramped down, the artery diameter reduced and therefore the interaction between the stent and the artery occurred when the contact between stent OD and the artery surface was established. This portion of analysis placed strain on the stent as a function of the pressure on the stented artery. Fatigue strains were then determined by locating the strains at different pressures. Clearly the alternating strain was dependent upon the vessel compliance and the pressure differential. The mean strain, on the other hand, was dominant by the amount of oversizing. Our calculation indicated that the Cordis-NDC SMART^{TM} family of stents had a mean strain from 1% to 2% per their product IFU.

In addition to fatigue strains, one can also obtain the stent diameters at different pressures. In our studies on several Nitinol self-expanding stent product lines, FEA predictions of stent diameters agreed extremely well with the actual lab measurement of the stent diameters. These built confidence on the fatigue strain predictions [24].

To establish a fatigue baseline (a strain-life curve) for stent application, the test specimen must have similar deformation patterns to the deformation of a stent *in vivo*. A direct and efficient way to establish the strain-life curve for a stent is to perform fatigue testing on its individual struts. However, such "unzipped stents" are not easy to handle experimentally. We therefore built a unit cell of a stent, i.e., a diamond shaped specimen, to overcome the handling difficulties (Figure 7). It was designed to be similar to the strut geometry from several commercially available stents. The small holes in the ends of the sample were to assist in alignment and gripping the sample. The samples were processed in the same manner as a stent so that it had the same A_f and electropolished surface finish. They were stretched and compressed before the actual fatigue test and the load and displacement were recorded to ensure the processing consistency in sample preparation [22].

FEA was used to calculate the strain field in the specimen so that the test could be planned at the most relevant *in vivo* conditions for stent application; the results were interpreted as a strain-life curve [22]. Notice that when only the loading portion of the curve was considered, one could simplify the stress-strain curve as piecewise linear. Under this simplification, the beam theory was used to estimate the maximum strain inside the specimen and predict the load-displacement relation on

the loading path to confirm the FEA. Figure 8 shows that the theoretical prediction, FEA, and the experimental data agreed closely.

Fatigue tests were performed during the past two years and the test results were presented in reference [17]. By using the same analysis code and controlling the same process procedures, we were able to ensure fatigue safety. Accelerated device tests performed on several stent product lines have confirmed our predictions.
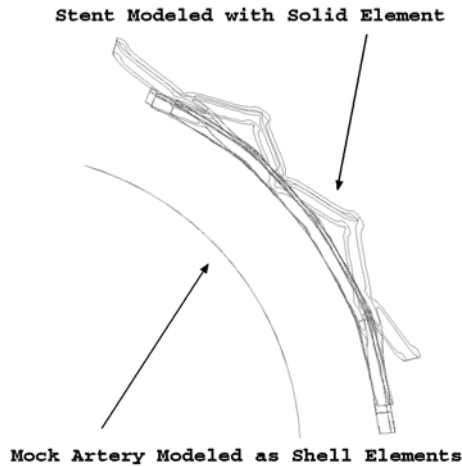
Figure 6 FEA model for stent fatigue strain analysis includes multiple rows of struts to cover the end effects and an artery to simulate the stent-artery interaction.

Figure 7 Diamond shaped specimen for fatigue study.

CONCLUSION

From two typical minimally invasive medical device applications, we showed that nonlinear FEA has opened the door for Nitinol engineering evaluations. This indicates it can be used as a predictive tool prior to prototyping the designs to optimize the device functionality, not only by varying the geometry of the design, but also by tuning the material properties. In addition, FEA can identify the fatigue strains at given *in vivo* conditions. This approach also addresses the device's fatigue life, which is essential for most implantable devices, provided a strain-life curve has been established from the same FEA to ensure consistency. To summarize, the use of FEA helps one to understand the device functionality and the fatigue properties of Nitinol. Experiments coupled with FEA can guide the device designer in improving service life and optimizing the device functionality.
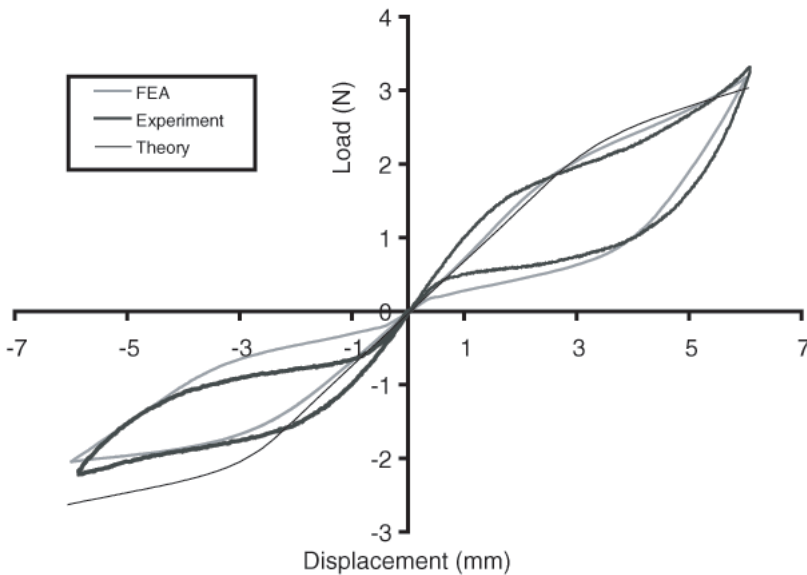
Figure 8 Comparison of FEA, theoretical prediction, and experimental data of load-displacement relation on a diamond-shaped specimen.

REFERENCES

1. D. Stoeckel, *Min, Invas. Ther. & Allied Technologies* **9** No. 2 (2000), p. 81.

2. D. Stoeckel and A. Melzer, *Materials in Clinical Applications*, eds. Vincenzini, P. and Techna Srl (1995), p. 791.

3. S. Miyazaki in *Shape Memory Materials*, eds. K. Otsuka and C.M. Wayman (Cambridge University Press, 1999), p. 267.

4. NDC web site, *www.nitinol.com*.

5. D. Tolomeo, T. Slater, and P. Wu in *SMST-2000: Proceedings of the International Conference on Shape Memory and Superelastic Technologies*, eds. S.M. Russell and A.R. Pelton (Pacific Grove, Calif.: International Organization on SMST, 2000), p. 517.

6. L. Anand and M. Kothari, *J. Mech. Phys. Solids* **44** (1996), p. 525.

7. F. Auricchio and R.L. Taylor, *Comput. Methods Appl. Mech. Engrg.* **143** (1996), p. 175–194.

8. F. Auricchio, R.L. Taylor, and J. Lubliner, *Comput. Methods Appl. Mech. Engrg.* **146** (1997), p. 281.

9. M.A. Qidwai and D.C. Lagoudas, *Int. J. Numer. Meth. Engng.* **46** (2000), p. 1123.

10. J. Knowles, *Comput. Mech.* **22** (1999), p. 429.

11. E. Patoor, A. Eberhardt, and M. Berveiller, *J. Phys.* **IV 6** (1996), p. 277.

12. Q. Sun and K. Hwang, *J. Mech. Phys. Solids* **41** (1993), p. 1.

13. Q. Sun and K. Hwang, *J. Mech. Phys. Solids*, **41** (1993).

14. N. Rebelo and M. Perry, *Min. Invas. Ther. & Allied. Technol.* **9** (2) (2000), p. 75.

15. N. Rebelo, M. Hsu and H. Foadian in *SMST-2000: Proceedings of the International Conference on Shape Memory and Superelastic Technologies,* eds. S.M. Russell and A.R. Pelton (Pacific Grove, Calif.: International Organization on SMST, 2000), p. 495.

16. X.-Y. Gong, A.R. Pelton, T.W. Duerig, N. Rebelo, and K.E. Perry in *SMST 2003: Proceedings of the International Conference on Shape Memory and Superelastic Technologies*, eds. A.R. Pelton and T. Duerig (Pacific Grove, Calif: International Organization on SMST, in press).

17. X.-Y. Gong, A.R. Pelton, and T.W. Duerig in *SMST 2003: Proceedings of the International Conference on Shape Memory and Superelastic Technologies*, eds. A.R. Pelton and T. Duerig (Pacific Grove, Calif: International Organization on SMST, in press).

18. J.P. O'Leary, J.E., Nicholson, and R.F. Gatturna in *Engineering Aspects of Shape Memory Alloys*, eds. T.W. Duerig, K.N. Melton, D. Stoeckel, and C.M. Wayman (1990), p. 477.

19. A.R. Pelton, J. Dicello and S. Miyazaki, *Min. Invas. Ther. & Allied. Technol.* **9** (2) (2000), p. 107.

20. A.R. Pelton, T.W. Duerig, and D. Stoeckel, *Designing with Nitinol* (Presented at SMST 2001, in Kunming, China, Sept. 2001).

21. T.W. Duerig and M. Wholey, *Min. Invas. Ther. & Allied. Technol.* **11** (4) (2002), p. 173.

22. T. Duerig, D.E. Tolomeo, and M. Wholey, *Min. Invas. Ther. & Allied. Technol.* **9** (3/4) (2000), p. 235.

23. S. Oh in *ABAQUS Users' Conference Proceedings* (Newport, R.I., June 2000), p. 535.

24. X.-Y. Gong, L. Zhu and A.R. Pelton (unpublished work).

FINITE ELEMENT ANALYSIS AND EXPERIMENTAL EVALUATION OF SUPERELASTIC NITINOL STENT

Xiao-Yan Gong,[1] Alan R. Pelton,[1] Tom W. Duerig,[1] Nuno Rebelo,[2] and Ken Perry[3]

[1]*Nitinol Devices & Components, 47533 Westinghouse Drive, Fremont, CA 94539*
[2]*ABAQUS West, 39221 Paseo Padre Parkway #F, Fremont, CA, 94538*
[3]*EchoBio, 579 Azalea Avenue NE, Bainbridge Island, WA 98110*

ABSTRACT

The mechanical properties of Nitinol stents are normally evaluated experimentally due to complexities resulting from large deformations and material nonlinearity. Despite difficulties associated with Finite Element Analysis (FEA), the success of computational analysis in combination with experimental study leads to better understanding of stent performance. This paper compares experimentally evaluated radial resistive forces of a Nitinol stent to predictions based on nonlinear FEA. The FEA was performed using ABAQUS with two user material subroutines independently developed specifically for Nitinol. Close agreements between the FEA and the experiments are shown for both user material subroutines.

KEYWORDS

NiTi, Finite Element Analysis, Superelastic, Crush, Stent, Radial Stiffness

INTRODUCTION

Recently, Finite Element Analysis (FEA) on Nitinol has been improved to cover superelastic behavior and has been proven to be a successful prediction tool in device design [1–6]. Among many successful applications, Nitinol self-expanding stents have drawn much attention. Compared to a balloon-expandable stent, a Nitinol self-expanding stent can be designed to provide constant gentle outward pressure, yet maintain high resistance to inward pressure and high crush resistance, in addition to its ease of deployment [7–8]. Because of these unique properties, demands for Nitinol self-expanding stents are increasing for certain applications.

The most important mechanical requirements for a stent are radial stiffness and fatigue life. Although both requirements can be evaluated through physical tests, they require "build-test" iterations and involve long-lasting fatigue testing. Thus, they can be very costly and time consuming. A

10-year device fatigue life under the heart rate of 75 beats per min. projects a 400 million cyclic pulsatile loading on the stent. Even with an accelerated fatigue test, a 400 million-cycle fatigue test can last months. FEA is an extremely useful complement and has proven to be effective and capable of providing a better, more detailed understanding of fatigue and design [9–10].

This paper discusses the results using two different approaches to modeling the superelastic constitutive behavior of Nitinol. Both approaches are then used in the analysis to determine the radial stiffness and crush characteristics of a Nitinol self-expanding stent. Comparisons with these tests confirm that FEA provides good predictions of the stent's mechanical response. Close agreement between two different constitutive approaches indicates FEA is a capable predictive tool in the early design phase of Nitinol devices.

CONSTITUTIVE MODELS

It is well known that Nitinol is a thermomechanical coupled material. Pelton et al. systematically demonstrated this thermomechanical coupled material response [11]. In their work, uniaxial stress-strain behavior of Nitinol wires was studied from –100°C to 150°C as shown in Figure 1. The series of stress-strain responses at different temperatures demonstrate the highly nonlinear, path and temperature dependent material constitutive behavior.
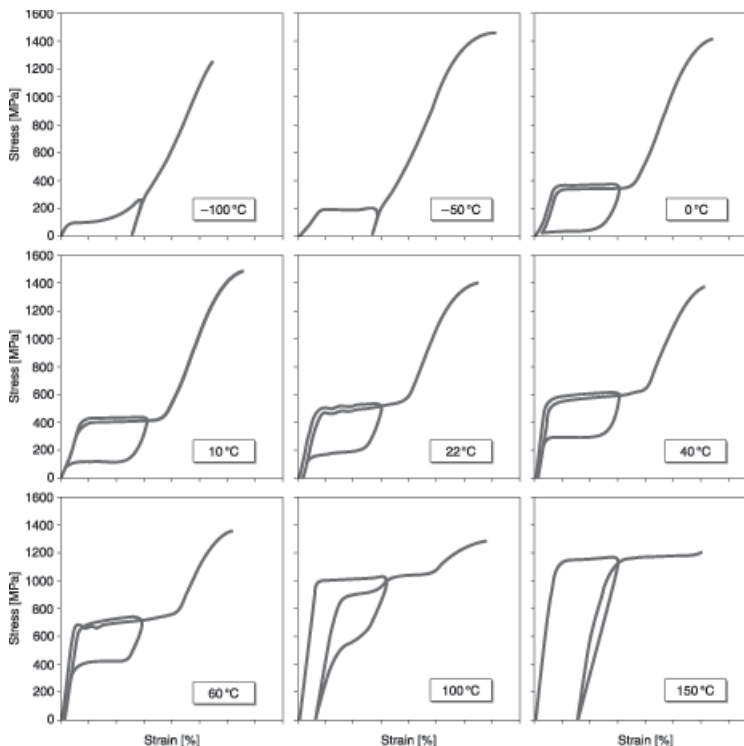

Figure 1 Uniaxial stress-strain relation at different temperatures.

Pelton *et al*. were also among the first to analyze the nonlinear material behavior of Nitinol using FEA, taking advantage of the available hyperelastic theory for rubbers [12]. This approach is very intuitive as Nitinol is, to some extent, a "rubber in the metal form." Despite their success, hyperelas-

tic theory is known to have stability issues that require more calibration tests (namely uniaxial tension, biaxial tension, and shear) to stabilize the model. Furthermore, the hyperelastic material model does not address the path and temperature dependent material behavior of Nitinol [13].

Over the last 10 years, many theories have been developed independently to account for the nonlinear path dependent thermomechanical constitutive behaviors of Nitinol [14–18]. They build the foundation for the state-of-art constitutive description of Nitinol. To date, advanced FEA on Nitinol has adopted those theories. The two constitutive models used in this paper are based on the approaches proposed by Auricchio et al. and by Qidwai and Lagoudas respectively [16–18]. For completeness, their approaches are briefly summarized below.

Auricchio's approach is based on generalized plasticity theory [16–17]. It models superelastic behavior of Nitinol, where any strain increment is decomposed into a linear elastic part and a stress-induced transformation part. The transformation part follows standard plasticity rules, such that strain increments can be derived from a plastic potential. The model includes transformation surfaces (analogous to yield surfaces) for both the austenite-to-martensite transformation and the reverse martensite-to-austenite transformation. ABAQUS West implemented this theory with modifications to allow for different elastic properties for austenite and for martensite, as well as different transformation stresses in tension and in compression. The loading can be either mechanical or thermal, and the transformation stresses (surfaces) are temperature dependent.

Qidwai and Lagoudas have developed constitutive models for shape memory and superelastic materials based on first principles [18]. In their approach, the second law of thermodynamics is written in terms of the Gibbs free energy. Strain, temperature, and martensite volume fraction become state variables that must satisfy the second law of thermodynamics. An evolution equation for the martensite volume fraction is derived from a dissipation potential and the effective transformation surfaces are evaluated as functions of the state variables. This approach also allows for different temperature-dependant elastic properties for austenite and martensite, and accommodates both mechanical and thermal loading. EchoBio developed a user-defined material subroutine based on this theory.

Both constitutive models need calibration based on a uniaxial tensile test. Figure 2 plots the comparison of the two independently developed constitutive models and the experimental result of Nitinol tubing that has been processed to achieve an austenite finish temperature (A_f) of 29°C and is tested at 37°C. Note that both models can be calibrated to predict the material's response well up to 8% strain based on a limited number of parameters. Discrepancy arises at higher strains because neither material model covers the plasticity in the martensitic phase. ABAQUS/Standard version 6.2-1 along with Nitinol UMAT/3D 3.24 (developed by ABAQUS West) and another user-defined material subroutine by EchoBio were used in the analyses.

RESULTS AND DISCUSSION

Radial Resistive Force (RRF) and Chronic Outward Force (COF)

RRF and COF are important mechanical responses unique to Nitinol Superelastic stents. RRF is the force generated by a stent to resist the reduction in its diameter and COF is the force generated by a stent when it self-expands from a smaller diameter towards a larger diameter. COF operates in the unloading portion of Nitinol's stress-strain curve while RRF operates on the loading portion of Nitinol's stress-strain curve. Generally speaking, RRF and COF are different and RRF is much larger than COF.
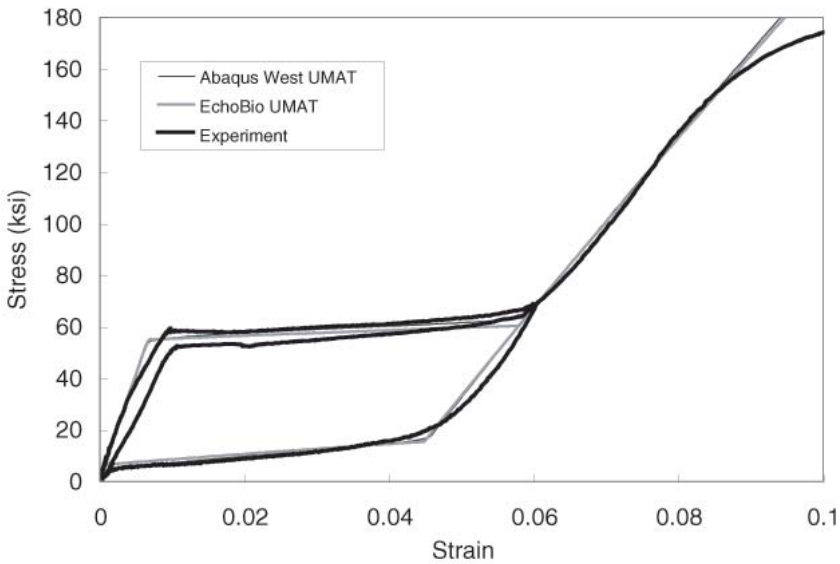
Figure 2 Comparison of FEA predictions and the experimental data.
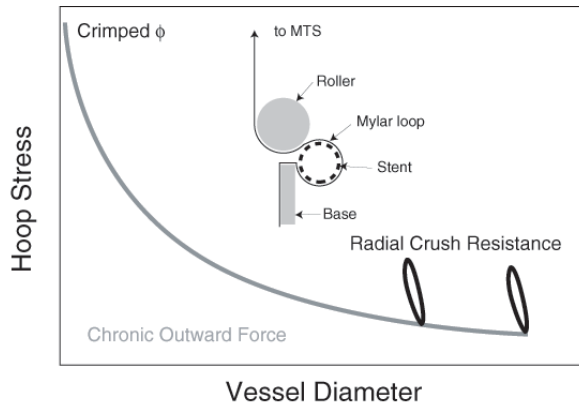
Figure 3 Schematic radial stiffness test setup.

Figure 3 illustrates schematically how these values are evaluated experimentally. Generally, this experiment is performed on an MTS system with customized test fixtures. In the first step, the stent is crimped down at a low temperature to a diameter of the delivery system. It is then placed inside the Mylar loop with one end of the loop fixed to the test fixture and another end connected to the MTS force actuator. The warm water of 37° C is then added so that the crimped stent is submerged at the constant body temperature. This causes the stent to produce an expansion radial force against the Mylar loop because the stent tends to recover back to its manufactured diameter. The Mylar loop then transfers the stent expansion force to the MTS load cell. By moving the MTS head down, one can release the pulling force and record the force as function of the head movement. The stent diameter change can be calculated based on the head movement. Thus, the force as a function of the

stent diameter is obtained. Notice that the recorded force comes from releasing the stent from its crimped diameter; therefore, it measures COF. At a given stent diameter when RRF is of interest, the MTS head is reversed to move up so that a pulling force on the Mylar is transferred to compress the stent down to a smaller diameter. This way, the RRF at this diameter is obtained. After the RRF is obtained, one can reverse the MTS head again to complete the test or can repeat the sequences to obtain the RRF at different stent diameters.

For simplicity, a two-strut model shown in Figure 4 is used in our FEA. For comparison purposes, the same model and mesh were used in the study. A 10 mm SMART Control^{TM} stent from Cordis self-expanding stent product line is selected for the RRF and COF study. In this model, symmetrical boundary conditions are applied to the open surfaces to maintain symmetrical deformation. User-defined rigid surfaces are used to compress and release the stent to the necessary stent diameters. The artificial stability option in ABAQUS/Standard is also turned on so that the analysis can run smoothly. The total strain energy and total artificial strain are traced during the whole simulation to ensure that the artificial energy is negligible.
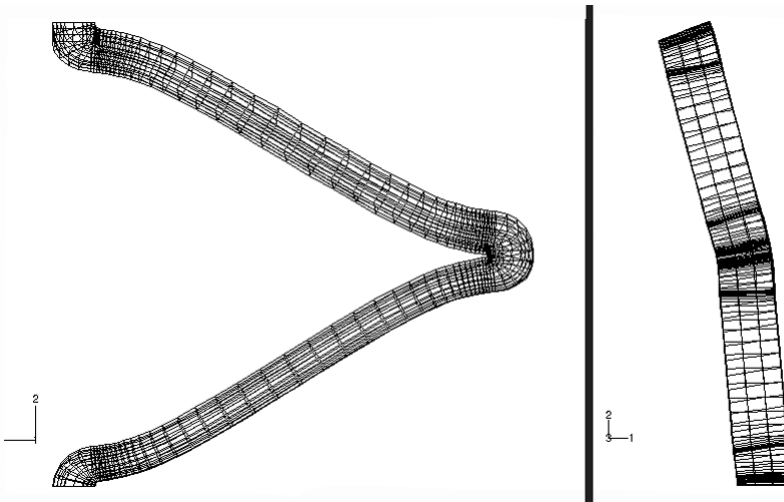
Figure 4 Side (left) and top (right) views of a two strut model.

Figure 5 shows the comparison between the FEA predictions and the test results. In both material constitutive models, the reload of the Nitinol is not simulated correctly. In addition, there are discrepancies at smaller stent diameters. This corresponds to the lack of a plasticity model at high strain in the martensitic phase in both material models; however, the COF agrees well with the experimental result at larger diameters. Luckily, larger diameters are of greater interests in stent applications. Furthermore, if one keeps in mind that RRF originates from the material response on the loading path, one can find the correct predictions of the RRF from the FEA results during the compression of the stent. Thus, even for these challenging results, the FEA solution agrees closely with the experimental results.

Figure 6 shows the strain contours on the deformed struts. The high strain locations identify the fatigue critical areas in stent manufacturing. Figure 7 plots the comparison of peak maximum principal strains for both material models. There is a close agreement between both material models and actual material behavior.

Figure 5 Comparisons of FEA predictions and the tests results.

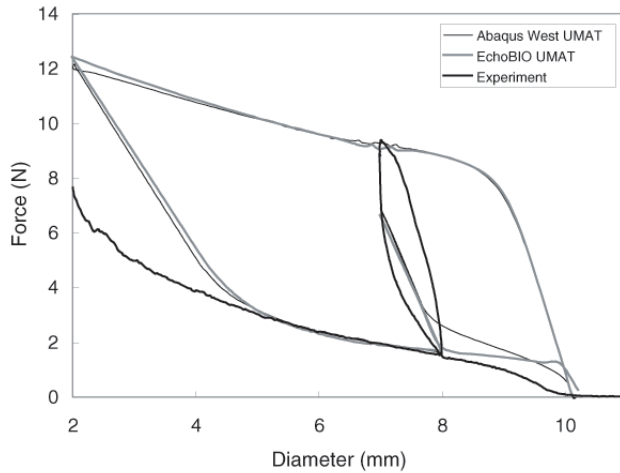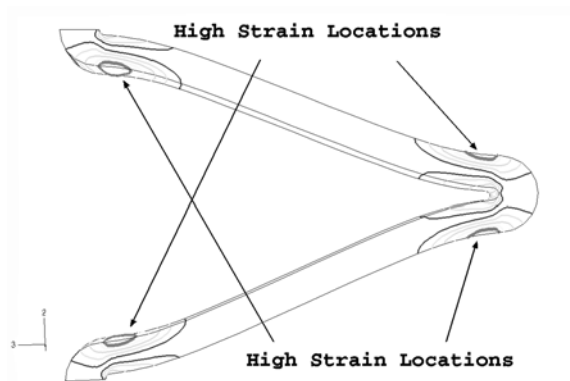*Figure 6 Maximum principal strain contours indicate the fatigue critical areas.*

Crush Resistance

The same diameter stent was chosen for the crush test. The crush test was performed on EnduraTec desktop tester ELF/3200 series, capable of higher displacement and load resolution. The test setup is straightforward. The stent was first deployed inside an 8 mm inner diameter (ID) 5% compliant tube (over 100 mmHg pressure differential) to simulate the worst case oversizing per the product IFU. The stented tube is then crushed between two rigid plates while the force and displacement were monitored. Air heating is used in this test. Environment temperature is 37° C to simulate the body temperature.

Figure 8 shows the FEA model for this simulation. Due to the repetitive patterns of a stent, only two half-row struts are used in the analysis. Axial and rotational repetitive boundary conditions are applied to the open ends of the model. The analysis involves rigid-to-flexible and flexible-to-flexible contacts over three steps. In the first step, all the contacts are removed so that the compliant tube, simulated as shell elements, is pressurized to expand to a diameter slightly larger than the stent outer diameter (OD). In the second step, the contact between the compliant tube and the stent
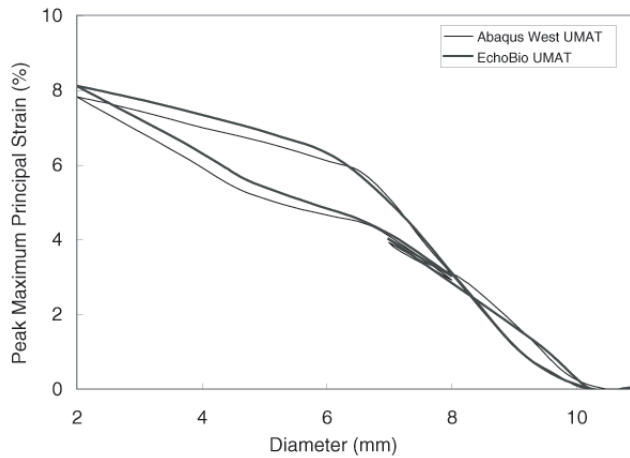
Figure 7 Peak maximum principal strain as function of stent diameter.
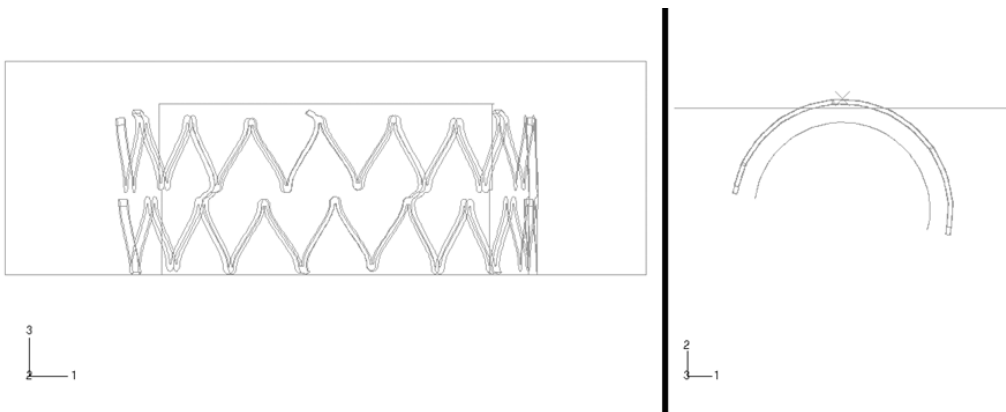
Figure 8 Side (left) and top (right) views of the FEA model for crush simulation.

OD is activated and the pressure acting on the tube ID is released completely so that the tube and stent reach their equilibrium positions. In the last step, contact between a rigid surface and the tube OD is activated so that the rigid surface can crush the stented tube. This simulation is difficult, not only due to the contacts and the material nonlinearity, but mainly because of the buckling of the stent. As a matter of fact, the buckling is visually observed both from the test and the FEA, as shown in the comparison of the deformed shapes from the experiment and the FEA in Figure 9.

Figure 10 plots the force-displacement response when the stented tube is crushed. Once again, good agreement between the FEA and the experiment indicates that both the material models represent the material response well. Yet FEA predicts lower force than actual measurement. This may be due partially to the test equipment compliance and partially to the lack of the input of the stress-strain response when Nitinol is subjected under compression. Figure 11 compares the peak maximum principal strain as function of the crush displacement for both material models. Once again, they agree closely.
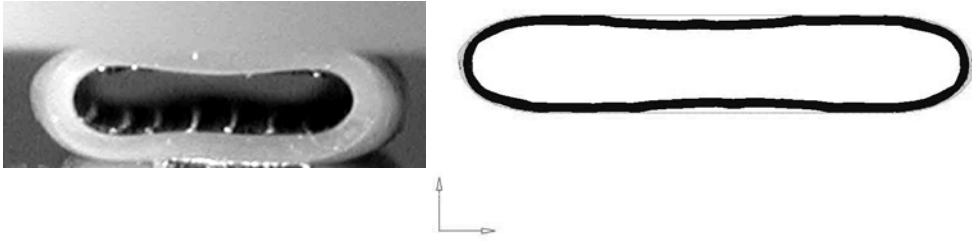
Figure 9 Comparison of deformed stent shape from experiment (left) and FEA (right).
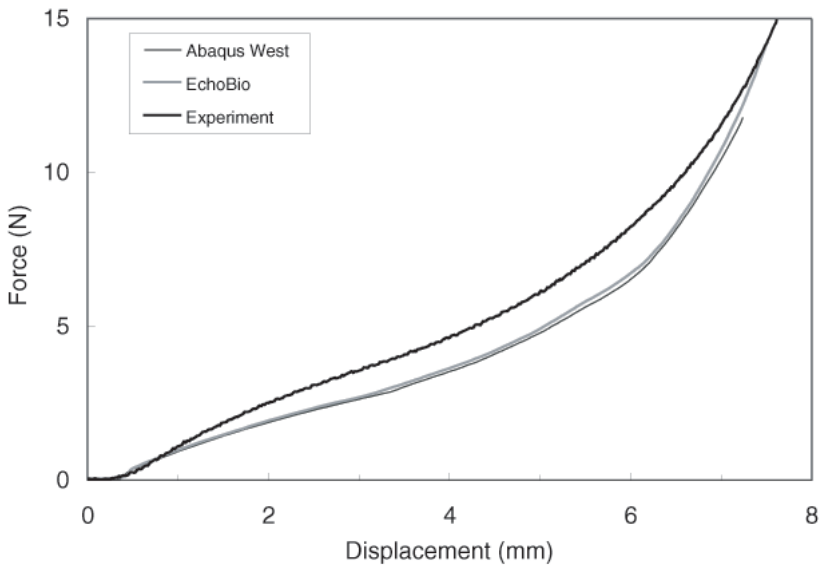
Figure 10 Comparison of force-displacement relations from experiment and FEA.

CONCLUSIONS

We showed that FEA, based on two different user-defined material subroutines, predicts consistent mechanical response for stents. Key results from FEA done with both material models agree well with experimental results, indicating that FEA is a powerful predictive tool that can be used in product development and design. Improvement of the material constitutive models for Nitinol is necessary to accurately describe the plasticity in the martensitic phase, as well as under multiple loading and unloading sequences.

REFERENCES

1. X. Gong and A.R. Pelton in *Proceedings of ABAQUS Users' Conference* (New Port, R.I., 2002), p. 1.

2. N. Rebelo and M. Perry, *Min. Invas. Ther. & Allied. Technol.* **9** (2) (2000), p. 75.
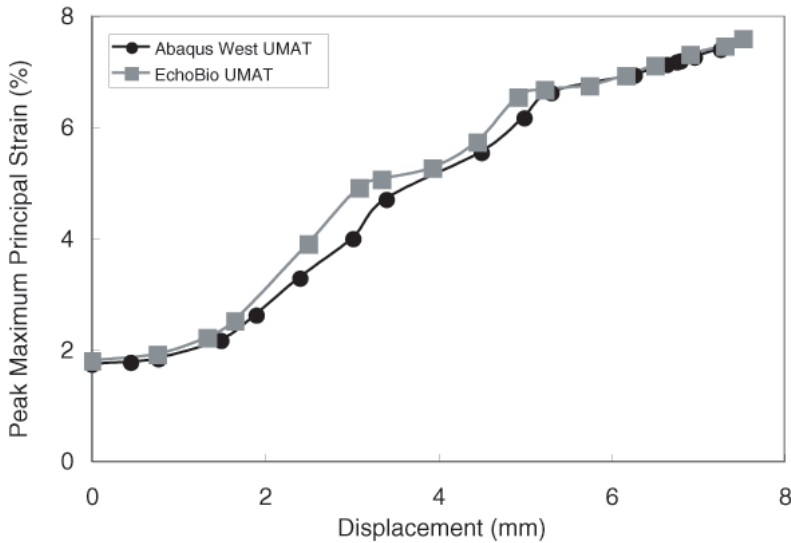
Figure 11 Peak maximum principal strain as function of displacement from two different material models.

3. N. Rebelo, M. Hsu, and H. Foadian in *SMST-2000: Proceedings of the International Conference on Shape Memory and Superelastic Technologies*, eds. S.M. Russell and A.R. Pelton (Pacific Grove, Calif.: International Organization on SMST, 2000), p. 495.

4. E. Patoor, Y. Gillett, E. Segard, and M. Berveiller in *SMST-97: Proceedings of the Second International Conference on Shape Memory and Superelastic Technologies*, eds. A.R. Pelton, D. Hodgson, S. Russell, and T.W. Duerig (Pacific Grove, Calif.: International Organization on SMST, 1997), p. 35.

5. F. Trochu and P. Terriault in *SMST-97: Proceedings of the Second International Conference on Shape Memory and Superelastic Technologies*, eds. A.R. Pelton, D. Hodgson, S. Russell, and T.W. Duerig (Pacific Grove, Calif.: International Organization on SMST, 1997), p. 595.

6. M.D. Perry and R.T. Chang in *SMST-97: Proceedings of the Second International Conference on Shape Memory and Superelastic Technologies*, eds. A.R. Pelton, D. Hodgson, S. Russell, and T.W. Duerig (Pacific Grove, Calif.: International Organization on SMST, 1997), p. 601.

7. T.W. Duerig and M. Wholey, *Min. Invas. Ther. & Allied. Technol.* **11** (4) (2002), p. 173.

8. T. Duerig, D.E. Tolomeo, and M. Wholey, *Min. Invas. Ther. & Allied. Technol.* **9** (3/4) (2000), p. 235.

9. D. Tolomeo, S. Davidson, and M. Santinoranont in *SMST-2000: Proceedings of the International Conference on Shape Memory and Superelastic Technologies,* eds. S.M. Russell and A.R. Pelton (Pacific Grove, Calif.: International Organization on SMST, 2000), p. 471.

10. C. Kugler, D. Maston, and K. Perry in *SMST-2000: Proceedings of the International Conference on Shape Memory and Superelastic Technologies,* eds. S.M. Russell and A.R. Pelton (Pacific Grove, Calif.: International Organization on SMST, 2000), p. 409.

11. A.R. Pelton, J. Dicello, and S. Miyazaki, *Min. Invas. Ther. & Allied. Technol.* **9** (2) (2000), p. 107.

12. A.R. Pelton, N. Rebelo, T.W. Duerig, and A. Wick in *SMST-94: Proceedings of the First International Conference on Shape Memory and Superelastic Technologies*, eds. A.R. Pelton, D. Hodgson, and T.W. Duerig (Pacific Grove, Calif.,1994), p. 353.

13. M. Pease and B. Walsh in *SMST-2000: Proceedings of the International Conference on Shape Memory and Superelastic Technologies*, eds. S.M. Russell and A.R. Pelton (Pacific Grove, Calif.: International Organization on SMST, 2000), p. 495.

14. R. Abeyaratne and J. Knowles, *J. Mech. Phys. Solids* **41** (1993), p. 541.

15. L. Anand and M. Kothari, *J. Mech. Phys. Solids* **44** (1996), p. 525.

16. F. Auricchio and R. Taylor, *Comput. Methods. Appl. Mech. Engng.* **143** (1996), p. 175.

17. F. Auricchio and R. Taylor, *Comput. Methods. Appl. Mech. Eng.* **146** (1997), p. 281.

18. M.A. Qidwai and D.C. Lagoudas, *Int. J. Numer. Meth. Engng.* **46** (2000), p. 1123.

FINITE ELEMENT ANALYSIS OF PLASTIC BEHAVIOR IN NITINOL

Nuno Rebelo,[1] Xiao-Yan Gong,[2] and Mike Connally[2]

[1] *ABAQUS West, 39221 Paseo Padre Parkway, #F, Fremont, CA, 94538*
[2] *Nitinol Devices & Components, 47533 Westinghouse Drive, Fremont, CA 94539*

ABSTRACT

Superelastic Nitinol can be plastically deformed under cyclic loading. Plasticity is well known to have an impact in the mechanical properties and fatigue resistance of metals and alloys. However, computational analysis of superelastic-plastic material response of Nitinol has not been commercially available to improve understanding of the complicated material response. A new version of the User-defined Material Subroutine (UMAT) Nitinol/UMAT model that applies to thermo-mechanical coupled superelastic plastic Nitinol has recently been developed. This article presents the single element test results of this Nitinol/UMAT using ABAQUS/Standard and the analysis of diamond-shaped fatigue test specimens. Results show that the new subroutine improves the Finite Element Analysis (FEA) result accuracy beyond the superelasticity limits.

KEYWORDS

NiTi, Superelastic-Plastic, UMAT, ABAQUS, FEA, Fatigue, Nonlinear

INTRODUCTION

With increasing successful applications in medical devices and implants, there has been an increasing demanding for better understanding of the complicated thermo-mechanical coupled behavior of Nitinol. The strong nonlinear material response also limits the valid applications of the traditional mechanical theory [1] and associated analytical method primarily based on linear elasticity or metal plasticity. Therefore, an effective and accurate analytical method capable of predicting the increasing structure response and material characteristics is necessary. Finite element analysis is the best candidate for this analytical quantitative evaluation application.

Pelton et al. analyzed the bending of Nitinol by modeling the nonlinear stress-strain response of Nitinol as a hyperelastic material [2]. Despite their initial success, new constitutive models are

501

necessary to better analyze the nonlinear stress-strain response and cover the thermo-mechanical coupled nature of material responses. With this increasing industrial demanding for this material constitutive modeling, a User-defined Material Subroutine (UMAT) Nitinol/UMAT specific for Nitinol was commercialized. Successful applications using this subroutine have been reported in the literature [3–5]. Recently, a study on the self-expanding superelastic Nitinol stent application using this approach has found good agreement with experiment evaluation and another independently developed material subroutine [6]. Consequently, nonlinear Finite Element Analysis (FEA) is routinely used as an up-front design evaluation tool and a quantitative evaluator to bridge the fundamental material studies to real life applications, such as the proper assessment of the fatigue and functionality issues [7]. Nevertheless, a better constitutive model beyond the superelastic limit is necessary, not only to complete the simulation to a wider strain range and improve the accuracy, but also for potential applications taking advantages of the plasticity or a better understanding of fatigue behavior.

PLASTICITY IN NITINOL

Plasticity in superelastic Nitinol occurs in any form of the Nitinol. Figure 1 and Figure 2 show the typical stress-strain responses of Nitinol wire and tube, respectively. Wick showed in his thesis that accumulation of plastic deformation by testing the same sample cyclically under uniaxial tension test with gradual increasing strain levels, as shown in Figure 2 [8]. The accumulation of the plasticity reduces the loading plateau stress and increases the Austenite finish temperature A_f.

(a)   (b)
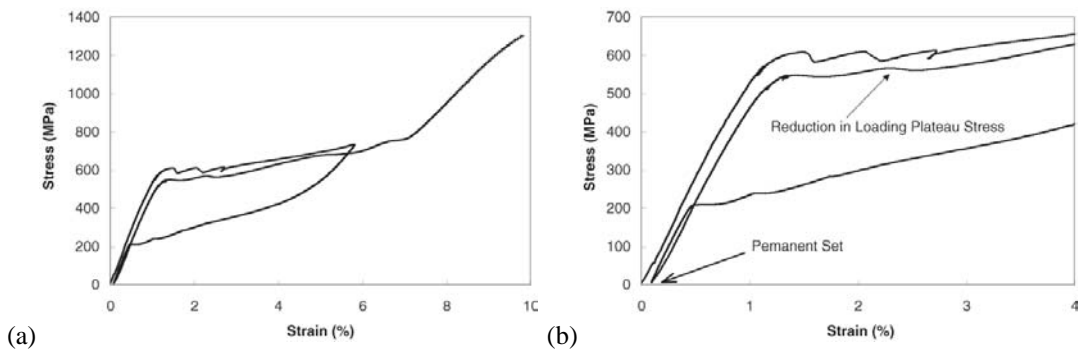
Figure 1 (a) A typical stress-strain response of a Nitinol wire under uniaxial tensile test. (b) Figure 1a plotted at small strain to show plastic deformation and decrease of loading plateau stress after the first load.

The irreversible plastic deformation, in general, can impact the design as the initial reference state varies when plasticity occurs. Pre-stressed metal components have been widely used in structural applications. There are also applications that take advantage of metal plasticity. Stainless steel balloon-expandable stents are good examples, where plasticity is used to increase the diameter of the stent from the size of the delivery system (e.g., 1–2 mm) to the diameter of the vessel (e.g., >3 mm). Normally, the expansion of a balloon expandable stent undergoes greater than 20% plastic strain [9].

Contrary to a balloon expandable stent, a self-expanding Nitinol stent is typically manufactured to a diameter 1 mm to 4 mm larger than the targeted artery. The stent is then radially compressed to fit into the delivery system. However, this compression may induce plastic deformation in critical regions of the stent. Depending upon the magnitude of the strain, the stent may not expand back to

Figure 2 (left) Uniaxial stress-strain response from Nitinol tubing also shows the plastic strain and decrease in loading plateau stress after the first loading, (right) Accumulation of plastic strain with cyclic loading (from [8] with permission).

its original diameter due to permanent set. Therefore, a prediction of the plastic deformation is necessary to address the recovery stent outer dia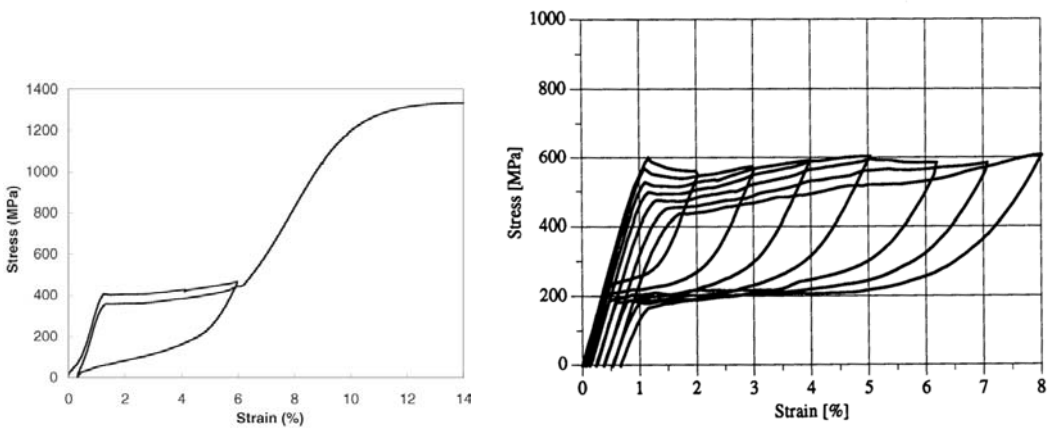meter and it opens the door for designs that may be able to take advantages of the shape memory and superelastic effects of Nitinol.

SUPERELASTIC-PLASTIC CONSTITUTIVE MODELING

The superelastic-plastic material model was developed with the plasticity of Nitinol at high strain in mind. As a starting point, plastic yielding is assumed to occur right after the completion of the austenite-to-martensite phase transformation, i.e., the end of the loading stress plateau. From then on, any additional loading produces plastic deformation.

The UMAT/Nitinol routine was originally written following the model proposed by Auricchio and Taylor [10,11]. This theory is based on the concept of generalized plasticity [12]. The theory has been extended to include plasticity effects. The strain is additively decomposed into three parts: a purely linear elastic component, a transformation component, and a plastic component. A rule of mixture is used to implement the change in linear elasticity from the austenite phase into the martensite phase.

The austenite to deformed martensite transformation is driven by the resolution of shear forces, and takes place within a range of stress levels that are characteristics of the material. This translates into the existence of a transformation potential, from which increments in transformation strain are derived, and active for well-defined levels of stress. The same is true for the reverse transformation, but at different stress levels. An assumption is made such that any change in stress direction produces a reorientation of the martensite with negligible additional effort.

Changes in temperature produce a shift in the stress levels at which the transformations take place. This shift is linear in temperature [13]. It has been observed experimentally that it takes less stress to produce the transformation in tension, and more in compression [8]. This is modeled with a linear Drucker-Prager-like approach for the transformation potential. However, the model may be non-associated if the user wishes to control the volumetric transformation strain. In such cases, the

transformation potential is different from the transformation surface defining the regions in stress space in which transformations may occur.

Similarly, the plastic deformation is also driven by the resolution of shear forces. We have assumed a purely deviatoric plastic potential, while the yield surface follows the same Drucker-Prager shape of the transformation surface. As stated above, the initial yield surface is assumed to coincide with the 100% martensite forward transformation surface. However, the yield surface expands with plastic deformation, producing a work hardening that follows the uniaxial tensile curve. This approach focuses on capturing the permanent deformation and the reduction in the tangential stiffness when the material is loaded beyond the loading stress plateau. This is chosen for ease of code implementation. The yield stress can later be customized once the systematic experimental data is available.

For simplicity, we assume negligible temperature effects in the plastic hardening curve. Therefore the increasing in the A_f due to the formation of the new dislocations and permanent deformation is also neglected.

In order to accommodate the large temperature effects observed in the transformation stresses, it is assumed that the permanent deformation at what appears to be the end of the martensite linear behavior is a material characteristic. This assumption that (during the first loading only) martensite that does not have an elastic range may produce too high plastic strains, as shown in the case study that follows, but it provides a good starting point and excellent agreement in the loading path of the complete stress-strain responses.

CASE STUDY

Single Element Test

To test the newly developed UMAT, we use the experiment data from uniaxial tensile tests on Nitinol tubing of $A_f = 29°C$ [6]. Figure 3 shows the comparison of the test data, calibrated FEA model with and without plasticity; as one can tell, it agrees well with the uniaxial tensile test even at very high strain levels.

Figure 3 shows the stress-strain relations under uniaxial cyclic load-unload sequences. Clearly, without plasticity, the material will respond along the same path regardless of the number of cycles. The addition of plasticity is capable of predicting the loading stress-strain response more precisely, as shown in Figure 3. Furthermore, it enables the formation of permanent set and at the same strain it results in reduction in both loading and unloading plateau stresses. The latter is more important in applications as it can not only predict the device functionality better, but also can help understand the impact of plasticity on the complicated fatigue behavior of Nitinol [6,7].

Pulling of a Stent-like Specimen

For simplicity and demonstration purposes, diamond-shaped fatigue specimens are used for demonstration of the new material subroutine when it is applied to multi-axial stress state. This specimen is very easy to handle and it resembles the deformation of a Nitinol self-expanding stent (Figure 4). Massive tests on the specimen has identified the fatigue characteristics of Nitinol and it is found that there are differences in the fatigue thresholds between the pushing of the samples and pulling of the samples. To better suit the stent application, it is suggested that the samples be tested under "push" conditions [7].
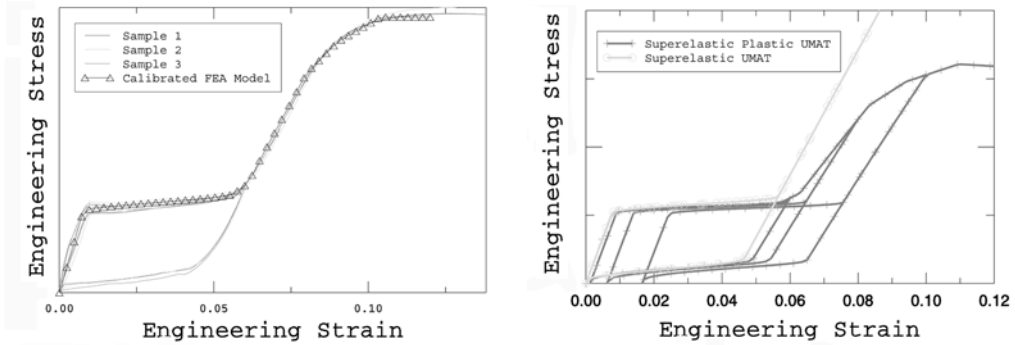
Figure 3 Calibrated material model is confirmed by experiment result (right) Comparison of the cyclic loading results of superelastic and superelastic-plastic material models.
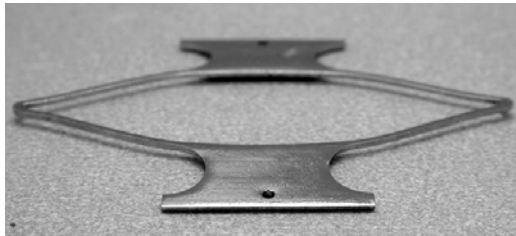

Figure 4 Diamond-shaped fatigue specimen.

For this study, the specimen pulled in tension to obtain the higher strains beyond the superelastic limit in order to compare the experiment results with the FEA prediction using the newly developed UMAT. The new UMAT was calibrated using the test data that was taken from the tube to have a same A_f with the diamond-shaped specimen.

Figure 5 shows good agreement between the deformed shapes from experimental displacements and FEA predictions. Figure 6 illustrates the comparison of the load-displacement experimental data with the relations predicted from Nitinol/UMAT with and without plasticity. The new UMAT with plasticity predicts a more accurate response at the higher strain level. Both UMATs predict the response well for the majority of Nitinol applications that are within the superelastic strain limits. The plastic deformation was overestimated when unloading the samples to its original state, as pointed out earlier. This overestimation is expected as the elasticity of the martensite phase was ignored in the current model.

CONCLUSION

We show from a simple application that the newly developed Nitinol/UMAT that includes plasticity predicts the experimental results well. As a starting effort to tackle the complicated plasticity of Nitinol, this is an excellent improvement to the existing Nitinol/UMAT that covers the superelasticity and thermo-mechanical coupled Nitinol material response. This new model opens the door for better understanding of the material response and further improvement for better super-elastic-plastic and thermo-mechanical coupled material response.
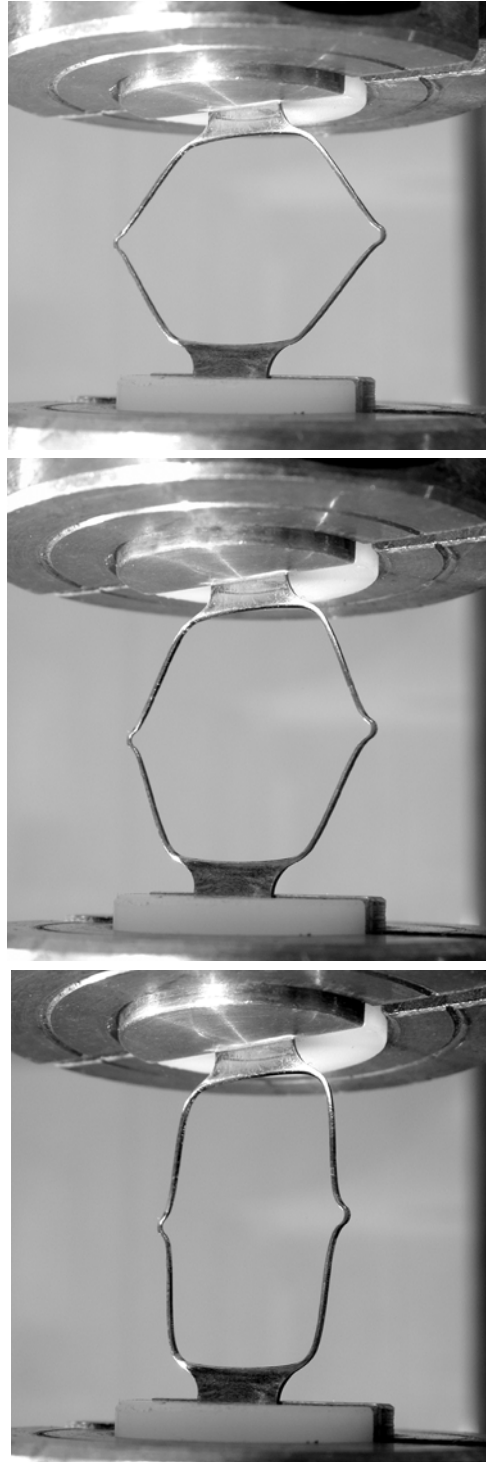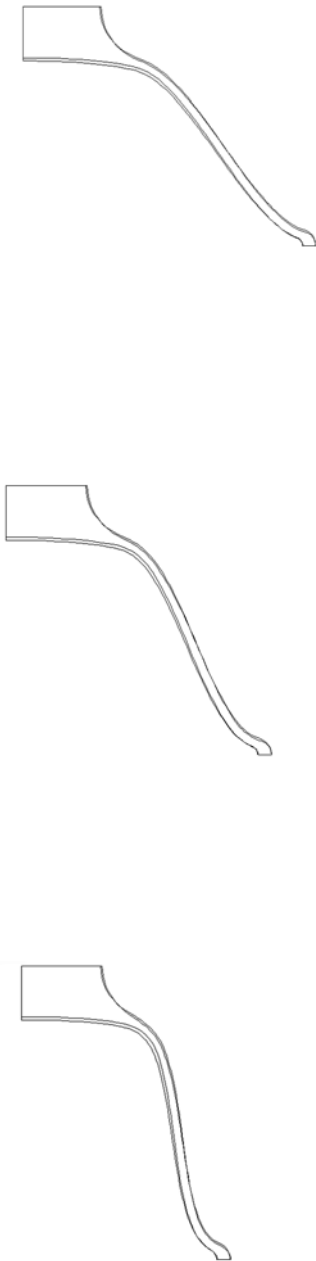
Figure 5 Deformed shape of fatigue specimen from FEA (left) and experiment (right).
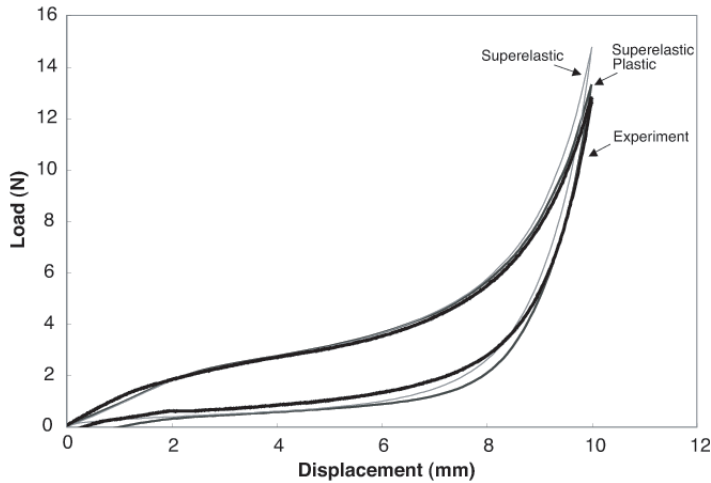
Figure 6 Load-displacement from FEA prediction and experiment.

REFERENCES

1.   S. Suresh, *Fatigue of Materials*, 2nd edition, Cambridge Press (1998).

2.   A.R. Pelton, N. Rebelo, T.W. Duerig, and A. Wick, in *SMST-94: Proceedings of the First International Conference on Shape Memory and Superelastic Technologies*, eds. A.R. Pelton, D. Hodgson, and T.W. Duerig (Pacific Grove, Calif., 1994), p. 353.

3.   X. Gong and A.R. Pelton in *Proceedings of ABAQUS User Conference* (New Port, R.I., 2002), p. 1.

4.   N. Rebelo and M. Perry, *Min. Invas. Ther. & Allied. Technol.* **9** (2) (2000), 75.

5.   N. Rebelo, M. Hsu and H. Foadian, in *SMST-2000: Proceedings of the International Conference on Shape Memory and Superelastic Technologies,* eds. S.M. Russell and A.R. Pelton (Pacific Grove, Calif.: International Organization on SMST), p. 495.

6.   X.-Y. Gong, A.R. Pelton, T.W. Duerig, N. Rebelo, and K.E. Perry in *SMST-2003: Proceedings of the International Conference on Shape Memory and Superelastic Technologies,* eds. A.R. Pelton and T. Duerig,(Pacific Grove, Calif.: International Organization on SMST), in press.

7.   A.R. Pelton, X.-Y. Gong, and T.W. Duerig in *SMST-2003: Proceedings of the International Conference on Shape Memory and Superelastic Technologies,* eds. A.R. Pelton and T. Duerig (Pacific Grove, Calif.: International Organization on SMST), in press.

8.   A. Wick, MS Thesis, University of Karlsruhe, Germany (1994).

9.   S. Oh in *ABAQUS Users' Conference Proceedings* (Newport, R.I., June 2000), p. 535.

10. F. Auricchio, R.L.Taylor, and J. Lubliner, *Comp Meth in Appl Mech and Engnrg* **146** (1997), p. 281.

11. F. Auricchio and R.L. Taylor, *Comp Meth in Appl Mech and Engnrg.* **143** (1996), p. 175.

12. J. Lubliner and F. Auricchio, *Int J Solids Struct*. **33** (1996), 991.

13. A.R. Pelton, J. Dicello and S. Miyazaki, *Min. Invas. Ther. & Allied. Technol.* **9** (2) (2000), p. 107.

A DECADE OF EVOLUTION IN STENT DESIGN

Craig Bonsignore

Cordis Corporation, Nitinol Devices & Components
47533 Westinghouse Drive, Fremont, CA 94539

ABSTRACT

Stents have been commercially available for vascular and nonvascular applications for well over a decade. In this time, hundreds of designs have evolved utilizing a vast array of materials and fabrication techniques, assuming myriad forms and geometries and including various additions. These categories of distinctions are presented as a pyramid of stent design options, highlighting key advantages or compromises within each category. Most commercial stent designs have attempted to differentiate themselves on the basis of stent geometry, so this diverse category receives particular attention. These categories are used to present an organized taxonomy of past, present, and future stent designs.

KEYWORDS

Stents, Design, Materials, Fabrication, Geometry, Nitinol

INTRODUCTION

The intravascular stent first rose to prominence in 1994 with the launch of the Palmaz-Schatz Coronary Stent. This new device transformed the practice of interventional cardiology, selling one million units in less than two years and creating a $700 million annual market nearly overnight. Today, the market for coronary stents alone has more than doubled to $1.5 billion, and is expected to immediately double yet again to $3 billion with the advent of drug eluting stents. The rapid growth of this market attracted hundreds of innovators, each seeking to match their perceived design advantages with a clinical need. This fertile environment spawned hundreds of clever, simple, revolutionary, and uninspired designs: "stent" appears in 5063 issued US Patents, 1225 times in the title. A recent survey uncovered 157 commercial stent designs, and countless others have certainly escaped the attention of this author and his able research team. The following pages will attempt to bring order to this menagerie of designs and offer insight into the design choices made by stent developers.

1977: PRE-STENTING

The word "stent" is attributed to Charles R. Stent, a nineteenth century English dentist, and was originally used to describe a mold for keeping a skin graft in place [2]. In a more modern context, the word "stent" refers to an implantable device used to provide structural support to a circulatory vessel or other luminal passage in human anatomy. Vascular stents evolved as an adjunct to balloon angioplasty, which was pioneered by surgeon Andreas Gruentzig in 1977. Minimally invasive angioplasty techniques became an important alternative to open heart surgery, but acute success and long term durability of such procedures was limited. Restenosis, or reclogging of treated arteries, was commonplace. This clinical problem was the impetus for developing stents and more exotic devices like intravascular lasers and drill-like burrs designed to ablate or remove the offending blockage. The first coronary stent implantation is credited to Jacques Puel and Ulrich Sigwart of Toulouse, France, in 1986.

The Palmaz stent would ultimately become the first to be proven successful in meeting the restenosis challenge. Dr. Julio Palmaz began his design exploration using the readily available resources of the day. His first stent prototype was created from copper wire and solder obtained from a local Radio Shack (Figure 2A). Knowing this design had its limitations, and inspired by the metal mesh used by a contractor doing plaster work in his house, Palmaz realized that similarly staggered slots could be applied to stent design. This would allow for fabrication from a single tube without overlapping filaments or solder points. Dr. Palmaz did not know how to go about creating such a slotted tube, so he did the only sensible thing: he consulted a rocket scientist in the rural woods of California. The retired German rocketeer suggested the second innovation, electrical discharge machining (EDM). These two central distinctive innovations of the Palmaz design led to its clinical success. Dr. Palmaz filed for a U.S. patent in November of 1985. After being rejected by every major medical device company in the field, he and his partners ultimately found an unlikely suitor for this controversial new technology. Johnson & Johnson had no experience in interventional therapy, but would ultimately become to first to commercialize this transformational new technology.

1994: RADIAL STRENGTH

In the early 1990s, there were a handful of stents in trials and commercially available. The primary types: The Wallstent, fabricated from braided wire of a cobalt alloy called elgiloy; The Wiktor stent, fabricated from tantalum wire formed into a helical ring structure; the Gianturco-Roubin Flex-Stent, fabricated from stainless steel wire in a clamshell design; and finally the Palmaz and Palmaz-Schatz stents, fabricated from slotted stainless steel tubes [2]. At this point, there were a growing variety of design options from which to choose (see Table 1).

Like most other experimental therapies of the day, three of the above designs were not successful in combating restenosis. But the Palmaz-Schatz stent proved to be different than the rest. In 1995, the BENESTENT trial clearly demonstrated the benefits of stenting; at last, interventional cardiologists had a tool that dramatically improved their success rates [3]. The slotted tube construction derived from the plasterer's mesh was the foundation for the stent's superior strength and clinical efficacy. As with most things unique and successful, the marketplace quickly responded with designs that attempted to emulate the attributes of the Palmaz-Schatz stent, while improving upon some of the shortcomings inherent in this first generation product.

Table 1 Stent Design Options

	Wallstent	**Wiktor**	**GR Flex-Stent**	**Palmaz/Palmaz-Schatz**
Material	elgiloy	tantalum	stainless steel	stainless steel
Form	wire	wire	wire	tube
Fabrication	braid	bend	bend	EDM
Geometry	braid	helical rings	clamshell	slotted tube
Figure	2B	N/A	2E (2nd generation)	2C

1995: FLEXIBILITY

By the mid 1990s, it was clear that stents were an essential (and profitable) new technology, and substantial resources were invested in development of next generation devices. From a clinical perspective, the strength lesson was clear, but strength often came at the expense of flexibility. Stent designers became focused on creating designs that would be more maneuverable in tortuous coronary anatomy, but still strong enough to provide adequate scaffolding for diseased vessels. EDM machining only worked well for straight slots, which made for a rather inflexible stent. It became clear that new technologies would be required if stents were to be made more flexible. Laser machining and photochemical etching answered the call, unlocking a virtually infinite world of geometrical possibilities for slotted tube stent designs.

Dr. Kobi Richter adapted the photochemical (PC) etching technology used in the electronics industry for stent manufacturing. His company, Medinol, went on to develop the NIR stent, which was PC etched from sheets of stainless steel, then wrapped into a cylindrical form and welded into a stent. The PC etching process allowed for the addition of flexible connector elements in the stent geometry, and also offered compelling economies of scale in production.

Also at this time, laser-machining capabilities were advancing rapidly. Laser micromachining quickly became the preferred fabrication technique for tube based stents, and remains so today. Laser fabrication technology allowed for virtually limitless variations in geometry, and became readily available to the stent development community through system integrators or vendors. Laser micromachining capabilities spawned the diverse variety of stent designs that have been created through the years.

While most of the stent designs in the second wave relied upon these new technologies for creating flexible and strong geometries, there is at least one notable exception. Arterial Vascular Engineering (AVE) developed a coronary stent of the very simplest construction, wire rings (Figure 2H), welded at some but not all junction points between adjacent bends. This perfectly simple construction proved to be quite successful. Its successors share the same construction and remain quite successful today. This design was one of the first to employ an open cell structure (Figure 1B) to achieve a successful balance of strength and flexibility.

1997: GEOMETRY

In October of 1997, Guidant received FDA approval for its MultiLink stent and became the first competitor to challenge J&J's 90% share of the U.S. market. Within 45 days, the MultiLink stent commanded 70% of the market. The Boston Scientific NIR stent and AVE MicroStent II followed in 1998, and these three new designs combined to render J&J's new Crown stent an insignificant player. It is worthwhile to consider the unique aspects of geometry that contributed to their fates.
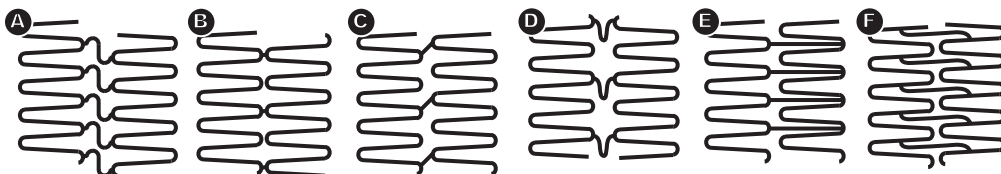
Figure 1 Typical stent constructions: (A) closed cell, peak-peak, flex connector, (B) open cell, non-flex connector, peak-peak, (C) open cell, nonflex connector, peak-peak, (D) open cell, flex connector, peak-peak, (E) open cell, nonflex connector, peak-valley, and (F) open cell, nonflex connector, midstrut.

First, a primer on stent construction: most stent designs have two fundamental constituents—expandable ring elements and connecting elements (Figure 1). Expandable rings are typically comprised of some number of struts arranged in a zigzag pattern with inflection points (tips or elbows) located at the end of each strut. Connecting elements (bridges), connect adjacent rings together, and may be described as flex or nonflex connectors, based on their shape. Connecting elements may also be described by the points at which they join with the ring elements. The terms, "peak-to-peak," "peak-to-valley," and "midstrut" can be used to describe these connection points. Stent designs may be classified as being open or closed cell, based on the arrangement of the connecting elements. A design may only be considered closed cell if each internal inflection point is connected peak-to-peak with a corresponding inflection point on the adjacent expandable ring. In this configuration, the closed area formed by two pairs of struts and two bridges is considered a cell. Any other configuration will feature some internal inflection points that are unconstrained, and the open cell would span one or more of these of these inflection points. Closed and open cell structures and a variety of bridge connection strategies are highlighted in Figures 1A–F [4].

The original Palmaz-Schatz stent and its successor, the "Crown" design are both examples of closed cell, nonflex connector, peak-to-peak designs which define the most inflexible of any possible stent configuration. The Crown stent, an innovation of Dean Kamen's DEKA Group, introduced a sinusoidal wave strut configuration that looked interesting, but did little to improve flexibility and was not very well received. The NIR stent was also a closed cell, peak-to-peak stent, but this design first introduced the flex connector. This V-shaped element did improve flexibility, and the stent became quite successful. The MultiLink stent introduced peak-to-valley connectors and open cell design. The peak-to-valley connections and open cell structure of this stent made it quite flexible; its successors continue to lead the market five years after its introduction.

1997: NITINOL STENTS

The above mentioned devices were all coronary stents, fabricated from 316L Stainless Steel. While the coronary market is the largest in terms of dollars, the peripheral vascular and nonvascular systems present a far greater variety of potential stent applications. For these applications, the clinical

requirements are quite diverse, but often necessitate stents of larger diameters that can recover from dynamic motions or outside forces. The carotid arteries of the neck, and superficial femoral arteries of the legs are both examples of vascular beds where plastically deformable stainless steel stents could become crushed and compromise blood flow. These indications demanded self-expanding, crush recoverable stents, and thus a different material. The Wallstent is a braided mesh type stent constructed from filaments of a cobalt based alloy [5]. It had been available since the early 1990s and developed a loyal following in spite of drawbacks including substantial length differences between its expanded and constrained states that made accurate placement difficult. It was clear that the unique superelastic properties of nickel-titanium (Nitinol) would be a benefit for many peripheral vascular indications, but the only Nitinol stents available were wire based, and were not particularly successful. In the mid 1990s, as laser cut stainless steel tube coronary stent became the standard, it became apparent that the same technology could be applied to Nitinol tubing.

Bard released the Memotherm in 1997 (Figures 2J), and Cordis released the SMART stent in 1998 (Figures 2I); both are examples of open cell, peak-to-peak constructions. The SMART stent became the dominant design in the endovascular marketplace, and remains the leader today. The success of the SMART stent design was largely due to its very fine mesh structure that offered exceptional contouring, flexibility, and apposition characteristics.

It is estimated that Nitinol stents now comprise 60% of the endovascular stent market. Nitinol stents also dominate nonvascular markets including urologic, upper and lower gastrointestinal, and trachea-bronchial applications.

DESIGN CHARACTERISTICS

Flexibility

Flexibility is often cited as the most important characteristic of any stent design. Flexibility usually implies deliverability, or the capacity for the unexpanded stent to navigate tortuous anatomy en route to its destination. Flexibility is also often associated with contourability, or the capacity for an expanded stent to assume the natural curve of a vessel without unnatural straightening. Both of these characteristics are fairly easy to observe, measure, and understand for physicians and stent designers alike. Some of the design characteristics impacting flexibility are as follows:

Cell Structure: Open cell structures are often substantially more flexible than closed cell structures, but require some compromises. First, when the unexpanded stent is placed in a tight bend, unconnected inflection points can lift up and present an irregular edge to the surrounding lumen—this is often described as fish scaling (Figures 2K). Second, when the expanded stent structure is placed in a bend, the unconnected inflection points can spread apart from each other, thus compromising scaffolding (Figures 2L).

Flex Connectors: Flex connectors add flexibility, but do so at the expense of scaffolding. The addition of flex connectors between expandable rings increases cell size, thus compromising scaffolding. More flexible flex connectors require increased spacing between expandable rings, and consequently decreased strength of the full structure.

Dimensions: Stent dimensions also play an important role in flexibility. Flexibility is inversely related to stent diameter, wall thickness, and the width of flex connectors.

Strength

Strength is arguably the single most important characteristic of stent design, and is perhaps the least understood. The FDA guidance document [6] defines radial strength as, "change in stent diameter as a function of circumferential pressure … noting the point at which deformation is no longer reversible." Stent designers have interpreted this in many ways: the external hydraulic pressure required to collapse a stented tube; the force required to crush a stent between flat plates; or the tension in a collar used to reduce the diameter of an expanded stent. Physicians, however, most commonly interpret the strength of a stent as the amount of *recoil* the vessel experiences after the stent is expanded. This creates another point of confusion, because the FDA guidance document (and stent designers) define stent recoil as the amount of elastic recoil experienced by a stent in the absence of any external loading. Superelastic self-expanding stents create further confusion in this area, as the concepts of nonrecoverable deformation and elastic recoil are meaningless. It is proposed that stiffness is a more appropriate and universal measure of the strength of a stent. In the stiffness interpretation, an expanded stent is constrained by a contracting collar and the tension in the collar is measured as a function of stent diameter. This tension can then be normalized by the length of the stent, and plotted against diameter. The slope of the resulting line relates to the stiffness of the structure, and corresponds with the physician's observation of stent "recoil" when loaded by a diseased vessel. The choice of materials and dimensions are the main factors that influence stent strength.

Material: The choice of material, its elastic modulus, and its stress-strain curve are key drivers of stent strength. Plastically deformed balloon expandable stents offer rigidity that cannot be matched by self-expanding Nitinol stents, for example. However, superelastic Nitinol provides a constant and gentle outward force over time, and can recover from crushing or other large deformations. Bioabsorbable polymer stents are compelling in theory, but have found limited success to date because of the fundamentally limited strength of these polymeric materials.

Dimensions: Once the material has been chosen, the strength of the design is dictated by the dimensions of the struts comprising the expandable ring segments of the stent. In most general terms, each strut has a length L, a width W, and a thickness T. These factors do not contribute equally to the strength of the stent. Strut width has the most substantial impact by far, followed by length, and finally wall thickness.

Scaffolding

Scaffolding is the third key design characteristic of stent design, and it is inexorably linked with strength and flexibility. Improving flexibility demands the ability for expandable ring segments to pull apart from each other on the outer radius of a bend and push together on the inner radius. Allowing this freedom requires disconnecting some inflection points, or connecting them with spring-like flex connectors. Both actions compromise scaffolding to some degree. Alternatively, scaffolding can be improved by decreasing the length of struts and placing more of them around the circumference. This creates more expandable ring segments along the length of the stent, and therefore decreases the amount of separation required between any two expandable rings to assume a given bend radius. This improves scaffolding and flexibility, but decreases strength.

A SURVEY OF STENT DESIGNS

The stent marketplace evolved in a Darwinian model, as innovators and opportunists bred the geometries of weak with the strong, peaks with valleys, and open with closed cells. A recent survey
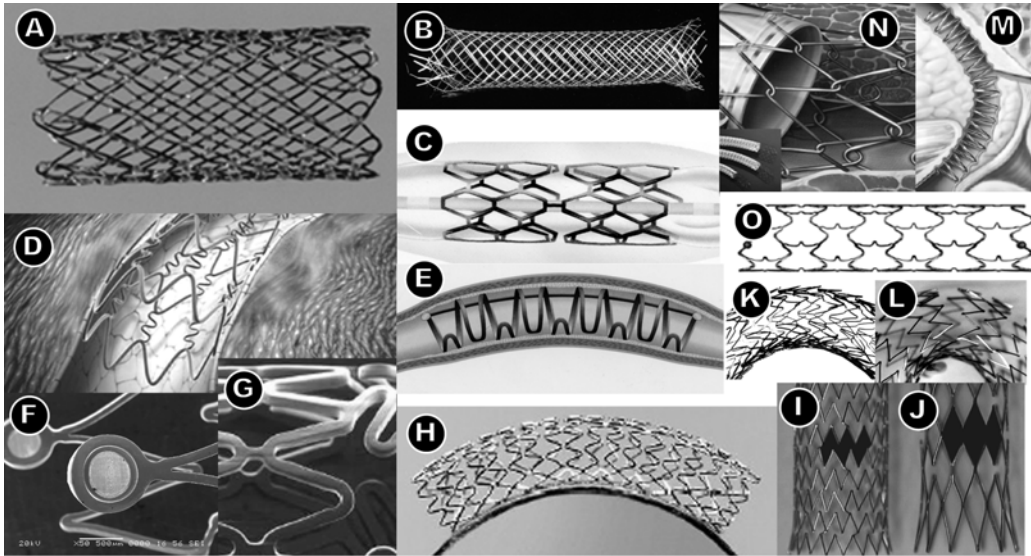
Figure 2 A variety of stent designs: (A) An early prototype of Dr. Julio Palmaz, (B) Braided Wall-stent, (C) Palmaz-Schatz Coronary Stent, (D) Cypher drug-eluting stent, (E) Gianturco-Roubin Flex-Stent II, (F) Radiopaque markers, (G) Combination of flex and non-flex connectors, (H) Welded ring AVE stent, (I) Nitinol SMART stent, (J) Nitinol Memotherm stent, (K) Dynalink peak-valley construction, (L) Open cell design with poor bend scaffolding, (M) Intracoil coil stent, (N) Nitinol wire stent-graf, and (O) Midstrut connection.
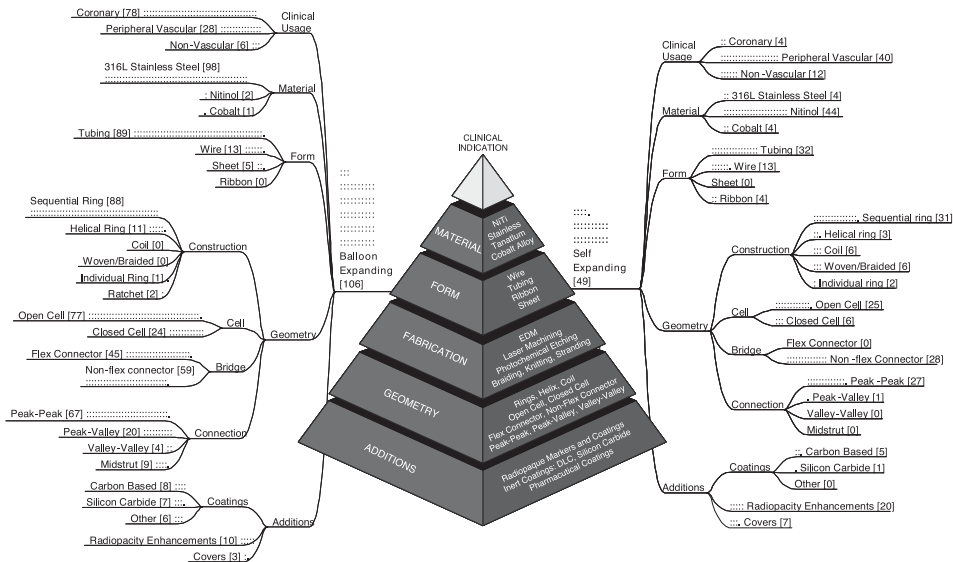

Figure 3 A survey of stent designs. Layers of the pyramid summarize the major design options faced by stent designers. Bracketed numbers depict the numbers of stent designs which fall in each of the described categories. These numbers are also graphically represented by dots on each branch. (:::::. = [9])

has revealed at least 157 stent designs that have been commercialized or are in development. Virtually every combination of peak, valley, and midstrut connection has been commercialized in the pursuit of the ultimate design. Hybrid designs even pack multiple design strategies within a single stent. These designs can be divided into balloon-expanding (BX) and self-expanding (SX) categories, then further classified by clinical indication. These categories are depicted graphically in Figures 3 and described in greater detail below.

Clinical Use: Coronary stent applications are overwhelmingly dominated by balloon expanding stents, while a majority of peripheral vascular and nonvascular designs are self-expanding.

Material: 316L stainless steel has been the material of choice for plastically deformed BX stents since the success of the Palmaz-Schatz stent in 1994, but there is a trend away from this material. Cobalt-based alloys are becoming increasingly popular for next generation BX stent designs, because they offer higher strength with less material. Nitinol dominates the SX stent designs, and its unique properties assure that it will to remain the material of choice for these applications for some time.

Form: Seamless tubing has been the most popular choice of material form since the success of the first slotted tube stents because of its profile advantages and continuous structure. This is true of both SX and BX designs, though in both cases several wire-based designs have proven viable and successful.

Fabrication: Laser micromachining dominates the current practice of stent manufacture of tube-based stents, though photochemical etching has been proven viable on tubes as well. The most intriguing development on the horizon is nanomanufacturing, which uses high vacuum sputtering techniques to build metallic vascular implants atom-by-atom in an additive fashion.

Geometry: Stent geometries have been very thoroughly explored in the past decade. Briefly describing each category:

> **Construction**: The sequential ring type of construction has proven most functional and popular for both plastically deforming and self-expanding stents. They offer the best combination of strength, flexibility, and small diameter for most vascular applications. Coil designs are quite popular for nonvascular applications—such as prostate and urethral stenting—because these designs are typically fully retrievable weeks or months after implantation. These coil type designs were never particularly successful in vascular applications because they are much larger in their constrained state than ring type designs.

> **Cell**: Despite the early success of closed cell geometries, open cell structures have proven successful and now dominate the BX stent designs 3 to 1. SX stents use open cell constructions almost exclusively. It is interesting to consider why this is the case. When designing with Nitinol tube, maximizing strength while minimizing diameter is often of paramount importance. Consequently, the designer must use as much material as possible in the expanding rings, leaving little if any room for effective flex connectors between the expanding rings. Since flex connectors are often not practical, Nitinol tube designs most often derive their flexibility from open cell construction and not from flex connectors.

> **Bridges–Connector Type**: The survey shows a nearly even split between balloon expandable with flex and with nonflex connectors; several featured a combination of both (Figures 3G). Flex connectors have been constructed in the shape of almost every letter of

the alphabet: "S", "N", "V", and so on. In self-expanding designs, flex connectors are virtually nonexistent for reasons noted above.

Connector Location: Peak-to-peak connection is the original and most common form of bridge connection, though alternatives are not uncommon. Different connection strategies can serve to improve flexibility and influence the foreshortening characteristics of a stent. Generally, peak-to-peak bridge connection will tend to draw adjacent expanding rings apart from each other as strut angles increase during expansion. This often results in foreshortening, or a reduction in length as the stent is expanded. Some designs feature flex connectors that are designed to stretch during expansion to reduce the tendency of the stent to shorten. Theoretically, valley-to-valley connection causes the opposite effect: adjacent rings will tend to push apart from each other, causing the stent to lengthen during expansion. Peak-to-valley connection counters these effects, and effectively eliminates the tendency for the stent to shrink or grow in length as it is expanded. It should be noted that the choice of bridge connection strategy could greatly impact the strength of a stent. A stent's strength is derived in large measure from the width of its constituent struts. The width of the struts is a function of the circumference of the tube and the utilization of the material around that circumference. Peak-to-valley, valley-to-valley, and midstrut connections require some circumferential material to be sacrificed from the struts—forcing a compromise in strength or profile. With peak-to-peak connections, however, no circumferential material is sacrificed. In Nitinol design, it is usually imperative to maximize the strength of the design, which explains the near exclusive use of this connection strategy in self-expanding stents in the survey.

Additions: This is the final frontier of stent design differentiation. Grafts or related covers may transform a simple stent into a device that performs some specialized function: exclude an aneurysm, repair a damaged vessel, or protect a lumen from tumor ingrowth. Such covered stents are more common among self-expanding stent designs. A variety of different types of coatings may be applied to stents. Usually, these claim to improve biocompatibility in some way, often purporting to decrease thrombogenecity or protect the body from metal ion release. Common coatings include diamond-like-carbon (DLC) and silicon carbide. These coatings are found on a handful of BX and SX stents. It is quite clear, however, that pharmaceutical coatings will play a profound role in the future evolution of stent designs. Heparin was the first commercially successful drug coated onto a stent. Similar to aspirin, heparin is generally administered systemically to reduce the risk of thrombus formation when the stent is first placed. A heparin coated stent effectively provides a biological non-stick surface, protecting the stent from attracting or collecting clot. The most recent developments in stent pharmaceutical combinations are antirestenosis drugs such as Sirolimus or Paxlitaxel that are combined with a polymer on the stent surface and designed to elute from the implant during the healing process. These drugs have been proven to dramatically reduce restenosis (reclogging of the vessel), and promise to make stenting an even more effective therapy in the treatment of coronary and peripheral vascular disease.

CONCLUSION

The history of stent design has demonstrated that each new device innovation is preceded by an enabling technology. Stenting itself was enabled by balloon angioplasty; EDM slotted tube technology brought us the first successful stent; laser micromachining enabled more flexible and easy to

use stents. Advances in the application of Nitinol opened the peripheral vascular world to the benefits of stenting. Incredible new pharmaceutical technologies now are being combined with implantable stents as we enter yet another dimension in successful minimally invasive interventional therapy. The next decade is certain to bring more sophisticated drugs in combination with more sophisticated devices, and likely new and transformational technologies as well.

REFERENCES

1. D. Stoeckel et al., *Min Invas Ther & Allied Technologies* **11** (4) (2002), p. 137–147.

2. R. Balcon et al., *European Heart Journal* **18** (1997), p. 1536–1547.

3. P.W. Serruys et al., *N Engl J Med* **331** (1994), p. 489–495.

4. D.R. McClean, *Reviews in Cardiovascular Medicine* **3** (Suppl 5) (2002), p. 516–522.

5. C.J. Pepine et al., *Journal of the Americal College of Cardiology* **28** No 3 (1996), p. 782–794.

6. *Guidance for the Submission of Research and Marketing Applications for Interventional Cardiology Devices: PTCA Catheters, Artherectomy Catheters, Lasers, Intravascular Stents* (US Food and Drug Administration, Centers for Devices and Radiological Health, May 1995).

7. *Handbook of Coronary Stents* 4th ed., eds. P.W Serruys and B.J. Rensing (Martin Dunitz Ltd, 2002).